Full Title: Myocardial Mesostructure and Mesofunction

Authors: Alexander J. Wilson[a,b] [0000-0002-5438-9707],

Gregory B. Sands[c] [0000-0002-7875-2099],

Ian J. LeGrice[c,d],

Alistair A. Young[e,f] [0000-0001-5702-4220],

Daniel B. Ennis[a,g] [0000-0001-7435-1311]

Affiliations:

a Department of Radiology, Stanford University, Stanford, CA, USA

b Stanford Cardiovascular Institute, Stanford University, Stanford, CA, USA

c Auckland Bioengineering Institute, University of Auckland, New Zealand

d Department of Physiology, University of Auckland, New Zealand

e Department of Anatomy and Medical Imaging, University of Auckland, New Zealand

f Department of Biomedical Engineering, King's College London, United Kingdom

g Veterans Administration Palo Alto Health Care System, Palo Alto, CA, USA

Running head: Myocardial Mesostructure and Mesofunction

Corresponding Author:

Alexander J. Wilson

Department of Radiology

Stanford University

1201 Welch Rd

Stanford, CA 94305

wilsonaj@stanford.edu

Keywords: cardiac anatomy, sheetlets, mesostructure, mechanics, diffusion tensor imaging

Word Count:

Abstract

The complex and highly organized structural arrangement of some five billion cardiomyocytes directs the coordinated electrical activity and mechanical contraction of the human heart. The characteristic transmural change in cardiomyocyte orientation underlies base-to-apex shortening, circumferential shortening, and left ventricular torsion during contraction. Individual cardiomyocytes shorten approximately 15% and increase in diameter approximately 8%. Remarkably, however, the left ventricular wall thickens by up to 30-40%. To accommodate this, the myocardium must undergo significant structural rearrangement during contraction.

At the mesoscale, collections of cardiomyocytes are organized into sheetlets, and *sheetlet shear* is the fundamental mechanism of rearrangement that produces wall thickening. Herein we review the histological and physiological studies of myocardial mesostructure that have established the sheetlet shear model of wall thickening. Recent developments in tissue clearing techniques allow for imaging of whole hearts at the cellular scale, while magnetic resonance imaging (MRI) and computed tomography (CT) can image the myocardium at the mesoscale (100μm to 1mm) to resolve cardiomyocyte orientation and organization. Through histology, cardiac diffusion tensor imaging (DTI) and other modalities, mesostructural sheetlets have been confirmed in both animal and human hearts. Recent *in vivo* cardiac DTI methods have measured reorientation of sheetlets during the cardiac cycle. We also examine the role of pathological cardiac remodeling on sheetlet organization and reorientation, and the impact this has on ventricular function and dysfunction. We also review the unresolved mesostructural questions and challenges that may direct future work in the field.

1. Introduction

The relationship between cardiac ventricular structure and mechanical function has long been recognized as important [1]. The orientation of cardiomyocytes changes from the epicardial surface to the endocardial surface in a helical manner, giving rise to the term *helix angle* [2]. Cardiomyocytes are heavily interconnected forming a continuously branching *syncytium* that contracts in near unison to pump blood efficiently. Cardiomyocyte connectedness is critical for spreading electrochemical signals throughout the heart to elicit coordinated mechanical contraction, and so the syncytial mesh poses a challenge for the integration of proliferating cardiomyocytes [3]. The cardiomyocytes are embedded within the myocardial extracellular matrix, which contains a range of proteins that contribute to structural and nonstructural functions (such as remodeling and angiogenesis) [4]. The structural components (e.g. collagen, elastin) form a scaffold that allows for effective transmission of forces throughout the heart, and also provides structural organization [5].

1.1. Multi-scale Structure and Function of the Heart

One of the challenges associated with studying cardiac structure and function is the contribution of features from vastly different structural scales (**Error! Reference source not found.**). At the scale of the whole organ (1mm to 100mm) clinical imaging with echocardiography, MRI, or CT measures: ventricular volumes and wall thickness; functional metrics such as ejection fraction, global longitudinal strain, and torsion; and tissue characteristics (e.g. perfusion and viability). At the cellular scale (10μm to 100μm) cardiomyocyte shape, cell-to-cell branching and functional features such as cardiomyocyte shortening, transverse thickening during contraction, and cell-to-cell

sliding (i.e. shear) underlie cardiac performance, but are currently difficult to measure *in vivo*. Between these two scales lies the intermediate *mesostructural* scale (100μm to 1mm) that is characterized by a continuously branching *syncytium* of cardiomyocytes collected into local sheetlets that is variously described by features such as cardiomyocyte helix angle, sheetlet orientation, sheetlet branching, the pathological fusing of sheetlets and loss of laminar organization, and extracellular matrix remodeling. These features impact sheetlet sliding mechanics, and the rearrangement of cells during contraction. Pathological remodeling also occurs at the ultra-scale, with remodeling of cardiomyocyte transverse tubules [6].

Cardiac mesostructure bridges the cellular and whole-organ scales, and is therefore critical for effective cardiac function [7]. For instance, measurement of mesostructural features such as aggregate cardiomyocyte direction impact the electromechanical performance of the heart [8], and provide important data for personalized computational models [9]. In general, there are many fewer studies at this mesostructural scale as compared with cellular and molecular, or whole-organ scales. Cellular-scale experimental methods focus on cardiomyocyte tissue culture, as well as preclinical studies examining the histology of various animal models of cardiac pathology. Organ-scale studies typically measure cardiac structure and function using CT, ultrasound, or MRI. Mesostructural studies are typically performed on *ex vivo* tissue, although recent developments in MRI push the limits of spatial resolution and microstructural sensitivity, thereby allowing for *in vivo* measurement of mesostructure [10]–[15]. Within the literature, studies of myocardial mesostructure often lack agreement as to the best imaging and analysis techniques, as well as a standardized way of reporting results.

Additionally, mesostructural studies can face the problem of registering *in vivo* and *ex vivo* image sets, or aligning data from different imaging modalities. These deficiencies in describing cardiac mesostructure in turn lead to inadequate computational models of the heart and severely limit their realism. However, this field has considerable opportunity for growth, and new technologies such as tissue clearing and MRI microscopy are becoming available to study the cardiac mesostructure in unprecedented detail.

1.2. Outline

This review focuses on the mesostructure of the heart, particularly the organization and deformation of aggregate cardiomyocytes and sheetlets through the cardiac cycle, and the contribution of these structures to normal function and pathological dysfunction. Section 2 details our current understanding of ventricular mesostructure, including a review of the orientation and extent of myocardial sheetlets. Section 3 reviews the different imaging modalities able to measure cardiac mesostructure, as well as their advantages and disadvantages. Section 4 reviews the mechanics studies that have linked myocardial sheetlets to ventricular strain. Section 5 examines the changes in myocardial sheetlet structure apparent during pathophysiological remodeling. Section 6 reviews recent developments in clinical translation of DTI that enable the measurement of aggregate cardiomyocyte orientation and sheetlet orientation that, when coupled with MRI methods to measure deformation, provide *in vivo* insight to the mechanisms of cardiac function and dysfunction. Finally, Section 7 outlines potential future work that would have a high impact on the field of cardiac mesostructure.

2. Cardiac Mesostructure

In this section we: (i) introduce the geometric reference frames used for understanding cardiac mesostructure, and the primary terminology; (ii) present and summarize the orientation and distribution of cardiomyocytes throughout the heart from a range of animal models (Table 1); and (iii) describe the laminar organization of the myocardial sheetlets.

The literature is full of discussions describing and debating the correct anatomical description, or model, of the heart. For an in-depth review of the various cardiac structural models we point the reader to the excellent reviews by Gilbert *et al.* [16] and Anderson *et al.* [17]. In this review we will focus on the laminar organization of myocardial sheetlets, which has been the predominant mesostructural model adopted by studies in this journal [18], [19], [28], [29], [20]–[27].

Cardiomyocytes form a continuously branching syncytium. As such, the term “myofiber”, which has previously been borrowed from skeletal muscle anatomy, is not suitable for describing the myocardium. We use the term *aggregate cardiomyocyte* to indicate properties of a collection of cardiomyocytes within an imaging voxel. For instance, the primary eigenvector of the diffusion tensor indicates the aggregate cardiomyocyte direction within an MRI imaging voxel (often 0.5mm-2mm in size).

2.1. Coordinate systems and angles

Systematically describing ventricular mesostructure requires the definition of coordinate systems and angles (**Error! Reference source not found.**). The “cardiac coordinate system” is most widely defined according to the left ventricular geometry with

circumferential, longitudinal, and radial directions (Figure 3). The longitudinal axis is defined as a line passing through the left-ventricular apex of the heart, as well as through the commissure between the left and right coronary cusps of the aortic valve [30]. In the short-axis plane (the plane orthogonal to the longitudinal axis), the radial (or transmural) direction extends from the center of the left ventricular cavity to the epicardial surface, and the circumferential direction follows the curve of the epicardial surface and is orthogonal to the radial and longitudinal directions.

Cardiomyocyte and sheetlet orientations are reported using the “myocardial coordinate system” (**Error! Reference source not found.**, microstructure) defined by the cardiomyocyte longitudinal direction (***f***), sheetlet (***s***) direction, and sheetlet-normal direction (***n***). For many use cases, such as computational modelling, these directions are assumed to be orthogonal, although there is no underlying anatomical reason for these directions to be strictly orthogonal. Various mesostructural angles relate the myocardial coordinate system to the cardiac coordinate system (Figure 2). The helix angle is the degree to which cardiomyocytes are angled out of the short-axis plane measured either using a projection of ***f*** onto the tangential plane (helix angle) or without projection (helical angle, Figure 2C). The transverse angle is the degree to which cardiomyocytes are angled with respect to the circumferential direction, measured either projecting ***f*** onto the short axis plane (transverse angle), or measured without projection (intrusion angle, Figure 2E). Sheetlet orientation can be described with the elevation of ***n*** with respect to the short-axis plane (sheetlet elevation) or angled with respect to the radial direction (sheetlet azimuth, Figure 2F). Sheetlet orientation can also be described

using the projection of the ***s*** onto the cross-fiber plane (secondary eigenvector angle, E2A, Figure 2D).

Glossary

Sheetlets: A group of cardiomyocytes approximately 4 ± 2 cells in thickness, arranged in a sheet-like structures [22]. Sheetlets branch and inter-connect with one another at the mesoscale (**Error! Reference source not found.**, Micro-scale structure).

Aggregate cardiomyocyte: Referring to properties of a collection of cardiomyocytes within an imaging voxel.

Cardiomyocyte direction (***f***): Direction aligned with the cardiomyocyte longitudinal axis (**Error! Reference source not found.**, Micro-scale structure).

Sheetlet direction (***s***): Direction perpendicular to the cardiomyocyte direction, but within the sheetlet plane (**Error! Reference source not found.**, Micro-scale structure).

Normal direction (***n***) : Direction perpendicular to both the cardiomyocyte and sheetlet directions (**Error! Reference source not found.**, Micro-scale structure).

Cross-myocyte plane: The plane normal to the cardiomyocyte long-axis direction (Figure 2B).

Helix angle: The angle between the circumferential direction and the projection of ***f*** onto the tangential plane (Figure 2C).

Helical angle: The angle between ***f*** and the tangential plane without projection (Figure 2C).

Transverse Angle: The angle between the circumferential direction and the projection of ***f*** onto short-axis plane. Historically known as the imbrication angle (Figure 2E) [31].

Intrusion Angle: The angle between ***f*** and the tangential plane without projection (Figure 2E).

E2A: The angle between the radial direction and the projection of the ***s*** onto the cross-myocyte plane (Figure 2D).

Sheetlet elevation: The angle between the radial direction and the projection of ***n*** onto the long-axis plane (Figure 2F).

Sheetlet azimuth: The angle between the radial direction and the projection of ***n*** onto the short-axis plane (Figure 2F).

Cardiac Axial Strains: Circumferential strain (E_{CC}), longitudinal strain (E_{LL}), and radial strain (E_{RR}) (**Error! Reference source not found.**, Macro-scale function).

Cardiac Shear Strains: Ventricular torsion or circumferential-longitudinal shear strain (E_{CL}), longitudinal-radial shear strain (E_{LR}) and circumferential-radial shear strain (E_{CR}).

2.2. Cardiomyocyte Orientation

The orientation of the cardiomyocytes throughout the heart is important for two principal reasons. Firstly, the principal cardiomyocyte direction indicates the principal direction of mechanical force produced by shortening of cardiomyocytes. Secondly, the cardiomyocyte direction indicates the principal direction of the electrochemical action potential spreading throughout the heart.

2.2.1. Helix Angle

When examined through the left ventricle, cardiomyocyte orientation changes as a function of depth [30], [32]. The transmural trend of this orientation is helical in nature, giving rise to the term “helix angle” [2]. Curiously, this means that mechanical shortening of cardiomyocytes has different orientations at different transmural locations. At first this seems to be counter-intuitive, as cardiomyocytes appear to be working in competition rather than cooperatively. However, longitudinally oriented cardiomyocytes are needed to produce >50% ejection fraction from the ~15% cardiomyocyte contraction [33], thus the variable direction of principal shortening produces effective contraction at the organ level. Additionally, the epicardial and endocardial cardiomyocytes form opposing spirals, contributing to efficient ejection [34]. The differing orientation of epicardial and endocardial cardiomyocytes, combined with their radial position give rise to tissue shear and ventricular torsion [35].

Key metrics for describing helix angle include the helix angle range (180° if cardiomyocyte orientation is -90° at the epicardium and +90° at the endocardium), as well as the transmural helix angle trend, which can be linear (Figure 3 in Ref 5) or tangent (Figure 4 in Ref 32) among others. By convention the epicardial cardiomyocytes have a negative helix angle, while the endocardial cardiomyocytes have a positive helix angle. A range of studies have reported helix angle range and trend across a number of animal models, and in general small animal hearts have a larger helix angle range compared with large animal and human hearts [36]. Anatomic studies of porcine hearts show helix angles of approximately -90° at the epicardium to +90° at the endocardium with roughly a linear trend [30]. However, studies in dog hearts show a helix angle trend

similar to a tangent function [32], with a rapid transition from longitudinally oriented cardiomyocytes towards circumferentially oriented cardiomyocytes.

Effective contraction of the heart at the organ level requires a combination of circumferential and longitudinal shortening, radial thickening and ventricular torsion. It is therefore likely that the transmural trend, and the frequency distribution of helix angles is important to normal heart function. Different transmural helix angle distributions have been observed between healthy and diseased hearts, between different animal models, across different regions of the heart, and between different imaging modalities. Transmural trends can be represented with helix angle frequency histograms: a tangent-type transmural trend produces a gaussian type frequency histogram, with a linear transmural trend producing a uniform frequency histogram.

Helix angle measurements show discrepancy between imaging methods, even within the same animal strain. For example, helix angle has been measured in the Wistar Kyoto rat using both Propagation-based X-Ray Phase Contrast Imaging (PB-X-PCI, Section 3.3) and diffusion tensor imaging [37][38]. Helix angle as measured by PB-X-PCI had a helix angle range of ~125° (epi = -50°, endo = +75°, linear trend), while the diffusion tensor study measured a helix angle of ~180° (epi = -90°, endo = +90°). Comparing these two studies, DTI over-estimated helix angle range (~55°) as compared with PB-X-PCI. Within Sprague-Dawley rat hearts, helix angle has been measured using both PB-X-PCI and DTI [39]. In this study PB-X-PCI slightly over-estimated the transmural helix angle range (12°) as compared with DTI. There are likely a number of factors contributing to these differences including sample preparation and fixation, the

time to imaging, the sample mounting medium or imaging solution, imaging parameters, image reconstruction workflow and structure tensor processing parameters.

2.2.2. Transverse Angle

Within the literature less attention has been given to the cardiomyocyte transverse angle, which is the degree to which cardiomyocytes lie within, or deviate from the epicardial tangential plane (Figure 2B). In terms of the organ-level contraction of the heart, cardiomyocytes that are oriented within the tangent plane (circumferentially rather than radially) contribute to both longitudinal and circumferential shortening, while cardiomyocyte cross-fiber thickening contributes to positive radial strain. However, a subpopulation of cardiomyocytes have been identified with a partial radial orientation, with some angles up to 45 degrees with respect to the tangential plane [40]. Histological findings of the subendocardium show that the transverse angle has a gaussian distribution centered on 30 degrees [41]. However, the presence of transverse cardiomyocytes was also investigated using extended volume confocal microscopy, and cardiomyocyte transverse angle was found to be uniformly zero across the LV free wall [42]. In a functional study by Lunkenheimer *et al.*, force probes measured the contraction through the cardiac cycle of transverse cardiomyocytes as well as tangential cardiomyocytes [43]. Transverse cardiomyocytes were found to have a different force profile as compared with tangential cardiomyocytes, and proposed as a mechanism to limit ventricular compliance during diastole. To our knowledge no other groups have confirmed this finding and it remains in need of further investigation.

Further evidence in wild-type mice found a change of transverse angle from positive at the base to negative at the apex [44]. Transversely oriented cardiomyocytes may

explain why E_{CR} shear varies longitudinally, from positive at the apex to negative at the base [45]. Additionally, mechanics simulation of the heart show that the inclusion of transverse angle is critical for correct estimates of E_{CR} – with a transverse angle of 25° providing the best match between experimental data and simulation [46]. In the absence of transverse cardiomyocytes, contraction of subendocardial cardiomyocytes produces a greater E_{CR} than is observed, suggesting that transverse cardiomyocytes contribute to the equilibrium of E_{CR}. There is a clear lack of research looking into the presence, importance, and functional contribution of cardiomyocytes with a large transverse angle. Studies that independently confirm the findings of Lunkenheimer *et al.* [43] would perhaps lead to more widespread appreciation of the importance of cardiomyocyte transverse angle [47], and its incorporation into biomechanical models of the heart.

2.3. Myocardial Sheetlet Mesostructure

At the mesoscale, the cardiomyocytes are bundled into sheetlets of 3-6 cells in thickness, giving rise to a layered or “laminar” structure [24]. This structural organization was documented, although perhaps not fully appreciated, by those studying the hierarchical collagen structure of the myocardium [48], which noted a collagen meshwork surrounding groups of cardiomyocytes approximately 4 cells in thickness. Although there is limited data on sheetlet thickness, both canine [24] and rodent hearts [21] exhibit a sheetlet thickness of ~4 cells, suggesting a degree of conservation across species.

Sheetlets are not independent entities, as they branch and inter-connect with one another at the mesoscale, via connections termed “muscle bridges” [49]. The early description by LeGrice *et al.* was later incorrectly interpreted as proposing sheetlet

layers that span the full ventricular wall without inter-connection. Such an organization may however lead to gross separation during filling. Along the sheetlet direction, sheetlets span approximately 250 μm, or approximately 15 cells [5] before they encounter structural features such as fusing with adjacent sheetlets, branching into two sheetlets, or abutments with sheetlets of a different orientation. Cardiomyocytes with a non-zero transverse angle (Section 2.2.2) would be cross between sheetlet structures, and therefore the presence of such cardiomyocytes would provide additional sheetlet connectivity. These structural branches and muscle bridges provide additional structural integrity to the myocardium. Additionally, extracellular matrix collagen provides mechanical integrity within sheetlets, and also couples adjacent sheetlets. Within sheetlets cardiomyocytes are surrounded by endomysial collagen [21], and within cleavage planes perimysial collagen strands connect adjacent sheetlets [5].

The regional orientation of sheetlet orientation was first systematically described in the dog heart by LeGrice *et al.* [24]. The sheetlet orientation can be examined in macroscopic long-axis views of the heart (Figure 3). These follow a general radial pattern – at the apex the cleavage planes (projected sheetlet direction) point towards the apex, while at the equatorial region cleavage planes align roughly with the short-axis plane, and at the basal region cleavage planes are elevated above the short-axis plane. These results are consistent with more recent measurements of sheetlets elevation using DTI and high resolution T_1-weighted imaging [50], [51], which show a sheetlet elevation of ~45° at the apex, ~0° at the equator, and ~-45° at the base.

However, sheetlet elevation alone does not capture the complex arrangement of sheetlets through the transmural span. Three dimensional imaging techniques are

318 therefore preferred, as the image volume can be re-sectioned transverse to the

319 cardiomyocyte long-axis at all transmural locations

[5], [42]. Virtual re-sectioning of a transmural LV section allows measurement of E2A, and revealed two populations of sheetlets [42]. The positive sheetlet population had an E2A centered on +60° in the subepicardium and midwall, and +30° in the subendocardium. The negative sheetlet population was centered at -30° through the transmural span, although most clearly defined in the midwall. Imaging of the left ventricle using DTI reveals a bimodal distribution of E2A, with the two populations of sheetlets: one at +30° and one at -30° [52].

The sheetlet azimuth is the angle between the radial direction and the projection of the sheet-normal vector onto the short-axis plane (Figure 2F). Sheetlet azimuth has an absolute value range of approximately 20 degrees from epicardium to endocardium, which is small relative to helix angle [50]. In general, the frequency distribution of sheetlet azimuth is gaussian and centered on zero [50]. In the basal anterior, anteroseptal, inferoseptal, and mid-anterior segments there is a small increase in sheetlet azimuth angle in the subendocardium. The basal inferolateral and mid inferolateral segments have a larger subepicardial increase in sheetlet azimuth.

2.4. Orthogonal sheetlet populations

LeGrice *et al.* (1995) noted that in various regions of the heart the laminar structure did not follow a single stack, but rather there were two populations of sheetlets [24]. The orientation of cleavage planes display discontinuities, producing herringbone patterns that are present in long-axis microscopy (Figure 3) of the RV and LV [53]. These are also revealed using extended volume confocal microscopy [54]. Additionally, the intersecting populations of sheetlets can produce parallelogram or rhomboid type aggregates of cardiomyocytes (Figure 3) [55].

Due to the presence of two sheetlet populations (**Error! Reference source not found.**), sheetlet orientation is not necessarily conserved across different individuals of the same species [18], [20], [56]. During systole, the myocardium has two principle orientations of maximum shear, and the sheetlet orientations align with these two shear directions [18]. Comparing two hearts directly can reveal conflicting sheetlet orientations, as individual hearts favor one predominant sheetlet population over the other [56]. Once sheetlet orientations from multiple hearts are pooled, a consistent bimodal distribution emerges that indicates the presence of two sheetlet populations.

It is still not clear the extent to which processing of myocardial tissue opens sheetlet cleavage planes, and whether one sheetlet population over the other is preferentially opened through this processing. Sheetlet cleavage planes have been demonstrated via high resolution MRI to be present without histological processing [57]. However, within a single myocardial tissue sample, imaging of consecutive histology sections can reveal a single sheetlet population in one section, but two intersecting sheetlet populations in the next section [58]. Additionally, DTI reveals no signal differences in tissue which, histologically, show one sheetlet population compared with those containing two sheetlet populations. It is possible that even in regions where only one sheetlet population is visible using histology, two sheetlet populations are present in the unprocessed tissue [58]. Histology processing may in some cases only render visible one sheetlet population, even if two are present.

Trying to capture information regarding hundreds of cardiomyocytes arranged into potentially two orthogonal sheetlet populations using DTI is not a straightforward task. Different sheetlet populations within a voxel may cancel out diffusion signal along the ***s***

366 and ***n*** directions, giving rise to non-physiologic data. A voxel containing two sheetlet
367 populations should theoretically produce an E2A that is almost parallel with the
368 tangential plane [13]. However, *in vivo* measurement of human hearts revealed an E2A
369 that is oblique with regards to the tangential plane, which is consistent with a single
370 predominant sheetlet population within a voxel [13]. Recent advances in diffusion MRI
371 encoding may provide more insight to intravoxel sheetlet organization.

First Author	Year	Imaging Method	Animal	Sample Size	Helix Angle	Transverse Angle	Sheetlet Elevation	Sheetlet Azimuth	E2A	Reference
Angeli	2014	DTI, *ex vivo*	Mouse, C57Bl6	5	✓	✓				[59]
Bernus	2015	DTI, *ex vivo*	Rat, Wistar	8	✓	✓	✓	✓		[57]
Teh	2016	DTI, *ex vivo*	Rat, Sprague-Dawley	5	✓	✓	✓	✓		[50]
Teh	2017	DTI, *ex vivo*	Rat, Sprague-Dawley	2	✓	✓	✓	✓		[39]
Haliot	2019	DTI, *ex vivo*	Human, Elderly	1	✓	✓	✓	✓		[60]
Giannakidis	2020	DTI, *ex vivo*	Rat, WKY	4	✓				✓	[38]
Giannakidis	2020	DTI, *ex vivo*	Rat, SHR	4	✓				✓	[38]
Carruth	2020	DTI, *ex vivo*	Rat, Sprague-Dawley	8	✓		✓			[61]
Carruth	2020	DTI, *ex vivo*	Rat, TAC	8	✓		✓			[61]
Magat	2021	DTI, *ex vivo*	Sheep	3	✓	✓	✓	✓		[51]
Ferreira	2014	DTI, *in vivo*	Human, healthy	11	✓				✓	[13]
Ferreira	2014	DTI, *in vivo*	Human, HCM	11	✓				✓	[13]
Sands	2008	EVCM	Rat, Wistar	1		✓			✓	[42]
Gilbert	2012	Histology	Rat, Wistar	4			✓			[23]
Garcia-Canadilla	2019	HREM	Mouse, WT	12	✓	✓				[44]
Garcia-Canadilla	2019	HREM	Mouse, Het	16	✓	✓				[44]
Garcia-Canadilla	2019	HREM	Mouse, Hom	28	✓	✓				[44]
Gilbert	2012	HR-MRI, *ex vivo*	Rat, Wistar	4			✓			[23]
Bernus	2015	HR-MRI, *ex vivo*	Rat, Wistar	8	✓	✓	✓	✓		[57]
Haliot	2019	HR-MRI, *ex vivo*	Human, Elderly	1	✓	✓	✓	✓		[60]
Magat	2021	HR-MRI, *ex vivo*	Sheep	3	✓	✓	✓	✓		[51]
LeGrice	1995	Nielsen Rig	Canine	2			✓			[24]
Teh	2017	PB-X-PCI	Rat, Sprague-Dawley	2	✓	✓	✓	✓		[39]

Table 1: List of anatomic studies measuring aggregate cardiomyocyte and sheetlet orientations. Mesostructural data has been measured from a range of human and animal hearts using various imaging modalities. Imaging abbreviations: diffusion tensor imaging (DTI), extended volume confocal microscopy (EVCM), high resolution episcopic microscopy (HREM), high resolution magnetic resonance imaging (HR-MRI) and synchrotron propagation-based x-ray phase contrast imaging (PB-X-PCI).

Animal/Patient abbreviations include: spontaneously hypertensive rat (SHR) and the Wistar Kyoto (WKY) rat, human hypertrophic cardiomyopathy (HCM), wild type mice (WT), Mybpc3-targeted knock-out heterozygous mice (Het) and homozygous mice (Hom).

3. Imaging of Cardiac Mesostructure

In this section, we review the imaging methods that have been developed to measure cardiac mesostructure. These include diffusion tensor imaging (Section 3.1), magnetic resonance microscopy (Section 3.2), micro computed tomography (Section 3.3), tissue clearing techniques for histology (Section 3.4), serial block-face histology (Section 3.5), ultrasound techniques (Section 3.6), and optical coherence tomography (Section 3.7). The imaging methods used to measure cardiac mesostructure are intrinsically linked with our understanding of it, and a long-standing goal in the field has been to measure both cardiac mesostructure and myocardial deformation through the cardiac cycle [62]. Of these, the ultrasound techniques (Section 3.6), as well as *in vivo* cardiac DTI techniques (Section 6) are the methods that are closest to achieving this.

3.1. Diffusion Tensor Imaging

Diffusion tensor imaging (DTI) measures the Brownian diffusion of water along many directions. Cellular structures restrict diffusion along certain directions, thereby providing information about the intravoxel tissue microenvironment [63]. DTI is used to probe diffusion lengths on the order of tens of microns, roughly the radius of a cardiomyocyte. DTI uses specialized MRI pulse sequences that include waveforms (i.e. modules) called diffusion gradients. When water diffuses along the direction of the applied diffusion gradient, the result is incomplete spin rephasing, and net signal loss (attenuation). An image without the applied diffusion gradients (termed the b_0 image) is also acquired, and this b_0 image provides a reference for measuring signal loss and the amount of diffusion along each gradient direction. The effective magnitude of the applied diffusion gradient is summarized by the waveform's b-value with units of s/mm^2 (reciprocal to the

units of diffusion, mm^2/s). As each acquisition only measures diffusion along a single direction, multiple directions are acquired to measure the diffusion in three dimensions. At least six directions are needed to reconstruct the intravoxel diffusion tensor. Eigen decomposition of the diffusion data provides the primary, secondary and tertiary eigenvectors, which correspond with the directions of greatest, next-greatest, and least diffusion, respectively.

To validate DTI as a tool for measuring cardiac mesostructure, previous studies have imaged the heart using DTI, subsequently imaged the myocardium using microscopy (the current reference standard for imaging myocardial mesostructure), registered the image data from the two methods, and compared the agreement of the mesostructural features. The DTI primary eigenvector (direction of greatest diffusion of water) has been shown to align with the aggregate cardiomyocyte direction [64]–[66]. Additionally, the DTI secondary eigenvector (direction of next-greatest diffusion) has been shown to align with the sheetlet direction [67], [68], and the tertiary eigenvector (direction of least diffusion) with the sheetlet-normal direction [58].

The invariants of the diffusion tensor have been utilized to estimate general microstructural features within a voxel. The two most commonly reported measures are the fractional anisotropy, and the mean diffusivity (also known as the apparent diffusion coefficient). The fractional anisotropy indicates degree of anisotropy of the diffusion, and a low fractional anisotropy has been shown to correspond with intravoxel dispersion of cardiomyocyte direction, as measured by histology [69]. A high mean diffusivity is correlated with an expanded extracellular volume [70], as is present in tissue with fibrosis.

3.2. Magnetic Resonance Microscopy

High-resolution T_1 weighted imaging sequences are able to resolve sheetlet mesostructure in *ex vivo* rat hearts using ultra high field MRI (imaging time ~24 hours) [23], [57]. One advantage of using high-resolution T_1 weighted imaging to validate DTI with myocardial mesostructure is that samples can also be scanned with both MRI sequences without moving the sample. The T_1 weighted images can be processed using a structure tensor approach, with eigenvectors defined according to spatial gradients in image contrast. This processing allows a direct comparison between anatomic structure tensors and diffusion tensors. Measurements of ***f*** and ***n*** from both DTI and anatomic structure tensors have been compared in detail [51], [57], [60]. The two measurements of ***f*** show excellent alignment. Although ***n*** shows good agreement on average, some regions had a difference of up to 60° between the two methods. The failure of the DTI ***n*** to completely describe the structure tensor ***n*** may be due to eigenvalue sorting problems (Section 6.4), or the presence of multiple sheetlet populations within a DTI voxel. Currently, it is clear that more studies are needed to characterize the correspondence of the structure tensor and DTI based estimates of mesostructure with those measured by histology.

3.3. Micro Computed Tomography

Micro-CT uses X-rays to image a sample from multiple orientations, allowing reconstruction of 3D image volumes. Imaging that relies upon x-ray absorption does not produce good contrast in cardiac tissue, as x-ray absorption in the heart is low relative to tissues such as bone. As such, metal-based stains such as iodine can be used to increase contrast in myocardial specimens. Alternatively, contrast in unstained tissue

can be boosted by acquiring phase-shift measurements (x-ray phase contrast imaging X-PCI), and this technique has been utilized in mouse hearts [71], and in human hearts [55], [72]. Micro-CT also allows some flexibility of preparation, samples can be imaged in paraffin, ethanol, or in air after solvent evaporation.

The signal-to-noise ratio of X-ray micro CT can be further improved through the use of high intensity synchrotron-generated X-ray beams. As such, synchrotron radiation-based X-PCI has been used to image whole rabbit hearts [73] (imaging time ~1 hour), and small blocks of human myocardium [55]. Such imaging methods are already revealing novel mesostructural features of the myocardium. For example, the orientation of myocytes within sheetlets have been shown to oscillate, and this a mesostructural feature that may contribute to sheetlet shear [55].

3.4. Tissue Clearing

Through a combination of lipid removal and refractive index matching, tissue clearing techniques prepare samples for microscopy and allow for imaging deep into thick tissue samples (hundreds of microns) [74]. Tissue clearing is particularly useful for producing high resolution microscopy image volumes, which are requisite for measurement of cardiac mesostructure. Tissue clearing methods are divided into hydrophobic and hydrophilic categories, each with their advantages and disadvantages. For detailed information regarding tissue clearing methods as applied to the heart, we refer the reader to a review by Sands *et al.* [74].

Light-sheet microscopy is particularly useful for imaging of cleared specimens. The method utilizes a focused plane of light to selectively illuminate a section of tissue (~5 microns in thickness). The illumination plane is scanned across the whole sample,

allowing whole rodent hearts to be imaged in ~30 minutes. Tissue clearing has a range of applications. In cardiac research, clearing allows measurement of cardiomyocyte disarray in human myocardial samples [75], it has been combined with transcriptomics to identify cell types within the cardiac conduction system at single-cell resolution [76], and light-sheet imaging has been used to perform cine imaging in zebrafish hearts [77]. This emerging method will likely play a very important role in further characterizing the mesostructure of the heart.

3.5. Serial block-face imaging

Serial block-face imaging is another technique that allows for 3D imaging of *ex vivo* hearts. After excision, hearts are fixed, stained, and embedded in preparation for a series of imaging and milling cycles. Depending upon the sample type and preparation technique, confocal microscopy can achieve imaging depths of tens of microns per imaging cycle. Embedded samples are mounted on a stage that allows both imaging and milling of the top surface. The top of the sample is imaged, and then milled to expose the next layer of tissue for imaging. The cycle of milling and imaging is continued until a volume of tissue has been imaged.

Extended volume confocal microscopy has been extensively applied to the heart, and has been utilized to describe the myocardial collagen structure in transmural sections of the left ventricle at resolutions less than one micron [5], [21], [42], [54], [78]. Other methods such as high-resolution episcopic microscopy have been used to assess the mesostructure of whole mouse hearts, and have in-plane resolutions of approximately 30 microns [44].

3.6. Ultrasound Techniques

Ultrasonic Backscatter Tensor Imaging is an ultrasound technique that allows for *in vivo* measurement of cardiac mesostructure [79], [80]. Multiple tilted plane waves are emitted, and a 2D receiver array receives the backscattered echoes. During image reconstruction, coherent compounding is used to generate a tensor for each voxel, which is used to measure aggregate cardiomyocyte orientation. This technique reveals changes in aggregate cardiomyocyte orientation through the cardiac cycle, and has interesting clinical potential.

Another technique, Echocardiographic Shear Wave Imaging, utilizes ultrasound shear waves that propagate more quickly along the cardiomyocyte direction than in the cross-myocyte direction. This imaging technique utilizes a linear array ultrasound probe, which is rotated through 180° in 5° increments. This process generates plane shear waves that propagate in a range of directions, allowing the aggregate cardiomyocyte orientation to be estimated [81]. The technique is able to reproduce the expected change in helix angle across the left ventricular wall.

3.7. Optical Coherence Tomography

Optical coherence tomography uses high intensity light to penetrate tissue, and measures structure from the backscattered light. The technique is able to provide 3D image volumes with a voxel size of <100 microns, with a penetration of several centimeters into tissue. Optical coherence tomography has been shown to be able to measure aggregate cardiomyocyte orientation [82], [83]. Optical Polarization Tomography is a variant of optical coherence tomography that has an improved

resolution and signal-to-noise ratio, allowing for tractography analysis. Measurements of ***f*** using this technique have been shown to agree with histology measurements [84].

4. Mesofunction: Sheetlet sliding as the mechanism of ventricular wall thickening

This section will review myocardial mechanics at the meso-scale (mesofunction), with a focus on the sheetlet sliding model of wall thickening, and the evidence supporting sheetlet sliding as the primary mechanism of ventricular wall thickening. Section 4.1 defines the whole organ cardiac strains as well as the meso-structural tissue strains. Section 4.2 covers the mechanics studies that link cardiac and mesostructural strain with sheetlet mesostructure (Table 2), and the role of multiple sheetlet populations in cardiac mesofunction. Finally, in Section 4.3 we review the passive mechanics of the orthotropic myocardium.

4.1. Cardiac Strain and Myocardial Strain

In the cardiac coordinate system, the three axial strains are: E_{CC} circumferential strain, E_{LL} longitudinal strain, and E_{RR} radial strain. During systole, shortening occurs along C and L directions, and therefore E_{CC} and E_{LL} are negative. R expands during systole, with E_{RR} typically having a positive value. There are also three shear-strains, the most well-known is the E_{CL} circumferential-longitudinal shear strain, also known as ventricular torsion. Additional shear strains include E_{LR} longitudinal-radial shear strain and E_{CR} circumferential-radial shear strain. At the mesoscale, there are three mesofunction strains: E_{ff} aggregate cardiomyocyte strain, E_{ss} sheetlet strain and E_{nn} normal strain. The six mesofunction shear strains (**Error! Reference source not found.**) are: myocyte-sheet (E_{fs}), sheet-myocyte (E_{sf}), normal-myocyte (E_{nf}), myocyte-normal (E_{fn}), sheet-normal (E_{sn}) and normal-sheet (E_{ns}).

4.2. Sheetlet mechanics studies

Early studies matched cardiac-level strains with mesofunction by injecting columns of radio-opaque beads into the myocardium, which were imaged using cine radiography [85]. By tracking the locations of these beads throughout the cardiac cycle, mesoscale strain was calculated. The principal direction of tissue deformation was observed to be orthogonal to the cardiomyocyte direction. Since cardiomyocytes only increase in diameter by approximately 8% during peak contraction, they concluded that significant mesostructural rearrangement of the myocardial tissue must occur in order to produce normal systolic wall thickening that exceeds 25% [85].

LeGrice *et al.* made use of the same methodology, with the additional detail of histological measurement of cardiomyocyte and sheetlet orientations in the myocardium containing the beads [86]. They found that the mesoscale strains aligned with shearing of the sheetlets, and proposed the sheetlet sliding model (Figure 1 mesofunction). This model purports that the sliding of sheetlets relative to one-another can account for up to 40% radial strain.

There are three components of wall thickening that arise from the sheetlets – (i) sliding of sheetlets relative to one another (i.e. mesostructural shear) (ii) the re-orientation or tilting of sheetlets, measured by changes in E2A, sheetlet elevation and sheetlet azimuth, and (iii) sheet thickening resulting from the thickening of constituent cardiomyocytes.

The involvement of sheetlet reorientation was further supported through measurements by Chen *et al.* (2005). They measured sheetlet orientations in both systole and diastole using both DTI and histology, and confirmed that sheetlets change their orientation

between different phases of the cardiac cycle [25]. Additionally, Ashikaga *et al.* found significant sheetlet strain during early diastole, supporting the idea that recoiling of sheetlets is an important component of early diastolic filling [28]. The organization of sheetlets allow for mesoscale shear: a resolution of forces produced from contracting cardiomyocytes both within and adjacent to a given sheetlet region [13]. DTI studies have demonstrated that sheetlets reorient during the cardiac cycle – measured as *E2A mobility* [12]. While some studies show negligible helix angle reorientation [12] others show evidence of helix angle changes during systole [10], [41], [43], [87]. Refer to Section 5.3 for further discussion of E2A mobility in diseased hearts.

Another feature of the myocardial mesostructure complicating the model of sheetlet sliding is the multiple populations of sheetlets. Sheetlet populations tend to be oriented approximately orthogonal to one-another, and produce a herringbone mesostructure of intersecting layers. This herringbone mesostructure deforms in a similar manner to an accordion (Figure 1 mesofunction), and allows for microscopic shear without the need for transmural shearing of epicardial and endocardial surfaces [88].

4.3. Passive Shear mechanics

Simulations of cardiac mechanics require, as input, the stress-strain (i.e. constitutive) properties of the myocardium. Myocardial stress-strain properties can be measured experimentally using devices that deform tissue samples, and measure the stresses required for such deformation. Myocardium is now accepted as orthotropic, with unique stiffness properties along ***f***, ***s****,* and ***n***. By mounting pieces of myocardium along different orientations, Dokos *et al.* measured myocardial shear stiffness [19] along the six mesoscale shear modes (Section 4.1). From their experiments, it was found that shear

591 modes that produced sliding of sheetlets had lower shear stiffness compared with other
592 shear modes, providing evidence that sheetlet shear facilitates mesoscale strain. These
593 findings have since been confirmed in human hearts [89].

594 One of the limitations of these studies is that the size of the myocardial samples are by
595 necessity much larger than myocardial mesostructural features. Li *et al.* addressed this
596 limitation by taking DTI measurements of the myocardial cubes, in order to match the
597 strain measurements with the mesostructural features [90]. These passive shear
598 experiments are important experimental data for validating computational models of the
599 heart. However, the identifiability of model parameters remains a problem even with
600 experimental data available, as parameters can differ by several orders of magnitude
601 between different myocardial samples. A comprehensive and well-validated model of
602 myocardial constitutive properties remains an open challenge in the field.

First Author	Year	Methods	Animal	Sample Size	Key Finding	Reference
LeGrice	1995	Cine X-ray, macro videography	Canine	10	Sheetlet shearing aligns with maximum strain vectors in the subendocardium.	[86]
Dokos	2002	Shear testing	Porcine	6	Shear modes align with sheetlet structures (NF/NS) that are the most compliant.	[19]
Sommer	2015	Shear testing	Human	28	Shear modes align with sheetlet structures (NF/NS) that are the most compliant.	[89]
Waldman	1988	Cine X-ray	Canine	7	The principal direction of deformation is orthogonal to the fiber direction, and therefore significant rearrangement of cardiomyocytes is required for ventricular wall thickening.	[85]
Li	2020	Shear testing	Ovine	5	Further confirmation of the orthotropic myocardial material properties.	[90]
Chen	2005	DTI ex vivo, histology	Rat, Sprague-Dawley	21	Hearts fixed in systolic and diastolic states showed reorientation of sheetlets.	[25]
Costa	1999	Cine X-ray, macro videography	Canine	6	Regional differences in wall thickening reflect underlying differences in sheetlet orientation.	[20]
Arts	2001	Mathematical model	Canine (Costa)	6	Sheetlets align with planes of maximum shear - two solutions exist, giving rise to the two populations of sheetlets.	[18]
Ashikaga	2004	Cine X-ray, histology	Canine	5	During early diastole, sheetlet strain decreases rapidly.	[26]

603 *Table 2*: Reference functional studies linking myocardial strain and mesostructure.

5. Sheetlet remodeling in disease

The link between mesostructure and function can become disrupted in disease states. In this section we review the studies of impaired mesofunction in a range of cardiac pathologies (Table 3). These include impaired mesofunction due to the loss of aggregate cardiomyocyte organization (Section 5.1), the loss of sheetlet organization and the fibrosis that fuses adjacent sheetlets (Section 5.2), and abnormal sheetlet reorientation (Section 5.3).

5.1. Loss of aggregate cardiomyocyte organization

Utilizing DTI, the fractional anisotropy (Section 3.1) can be measured, providing an estimate of the coherence of aggregate cardiomyocyte orientation. Fractional anisotropy measurements from diffusion tensor imaging have been shown to correlate with histological measures of cardiomyocyte splay [69]. HCM patients exhibit a lower fractional anisotropy as compared with healthy hearts [91], [92]. Additionally, when the HCM cohort was divided, those who suffered ventricular arrhythmia showed a significantly lower fractional anisotropy than the HCM patients that exhibited no arrhythmia [92].

A mesostructural feature that may contribute to impaired function is the loss of healthy helix angle profile. The presence of cardiomyocytes with a significant longitudinal orientation are thought to contribute to efficient ejection [33].While healthy hearts show a significant change in helix angle slope between systole and diastole, hearts with dilated cardiomyopathy do not show a significant change in helix angle slope through the cardiac cycle [11].

Acute myocardial infarction and its associated loss of tissue oxygenation leads to cardiomyocyte death, and eventual replacement fibrosis. Multiple studies have confirmed that infarcted myocardium has an increased mean diffusivity and a decreased fractional anisotropy [69], [93]–[98]. The mechanism by which mean diffusivity increases is thought to be the replacement fibrosis expanding the proportion of extracellular matrix relative to cardiomyocyte volume. Extracellular matrix is less restrictive of water diffusion and thus the expanded extracellular matrix within the infarct produces an increased mean diffusivity. Additionally, as cardiomyocytes have both mechanical and electro-chemical coupling, cardiomyocyte death resulting from acute ischemia results in a loss of cardiomyocyte organization. The loss of cardiomyocyte cellular organization (known as “fiber disarray”) in turn is thought to cause the decreased fractional anisotropy in the infarcted region.

Interestingly, the fractional anisotropy within the infarct is not entirely isotropic, and the remaining primary eigenvector is aligned with collagen structures within the infarct [99]. Pashakhanloo *et al.* found that within the infarcted myocardium, the *collagen* fibers (not cardiomyocytes) maintained a helix angle similar to the cardiomyocyte helix angle in healthy myocardium [93][69][100]. The helix angle transmural slope was steeper in the infarct region, thought to be due to wall thinning. Conversely, Sosnovik *et al.* [101] utilized a diffusion tractography approach and found that the infarct regions did not retain a normal transmural helix angle, but rather contained nodes of crossing fibers, which are absent from normal myocardium. Additionally, in hearts that have been infarcted, the remote zone may also undergo mesostructural remodeling [97]. In

particular, the helix angle becomes more right-handed, and this change is correlated with ventricular hypertrophy.

5.2. Loss of sheetlet organization

LeGrice *et al.* (2012) examined the progressive change in cardiac mesostructure in the spontaneously hypertensive rat model of hypertensive heart disease [21]. Utilizing extended volume confocal microscopy (Section 3.5), myocardial tissue was stained for collagen and imaged. These image volumes were able to show differences in collagen structures, as well as the sheetlet organization during the progression of disease. During late stage hypertensive heart disease, towards decompensated heart failure, the thickness of sheetlets increased, with a greater number of cardiomyocytes per layer (~6) compared with controls (~3). This fusing of myocardial sheetlets was associated with reduced fractional shortening at the ventricular level, measured using echocardiography. LeGrice *et al.* proposed that these abnormally thick sheetlets are less amenable to sliding, and less able to produce radial thickening required for effective ejection of blood.

Collagen deposition is another process that can lead to the fusing of sheetlets, and the loss of mechanically separated sheetlets (**Error! Reference source not found.**). During the phase of compensated hypertrophy the myocardium shows increased perimysial collagen deposition between sheetlets [21], [78], fusing sheetlet layers and limiting sheetlet shear. Treatment of hypertension with quinapril curtailed this deposition of collagen between sheetlets, and as such the number of cardiomyocytes per sheetlet in treated hearts was similar to those of control hearts (~3.5 cells per sheetlet), in contrast to the diseased hearts (~5.5 cells per sheetlet) [78]. Continued quinapril

671 treatment led to vastly different trajectories in terms of cardiac function, with treated
672 hearts showing significantly greater ejection fraction, reduced mean arterial pressure,
673 and improved rate of survival compared with diseased hearts.

5.3. Abnormal Sheetlet Reorientation

In hypertrophic cardiomyopathy (HCM), the heart wall becomes thickened and patients can progress to heart failure with preserved ejection fraction, irregular electrical activation, and sudden cardiac death. McGill *et al.* demonstrated the clinical feasibility of *in vivo* cardiac DTI in patients with HCM [102]. Further studies utilizing *in vivo* cardiac DTI in HCM patients demonstrated altered sheetlet dynamics in these patients [13]. In particular, the E2A mobility, which is the reorientation of sheetlets between systole and diastole, was diminished in HCM patients. E2A has been shown to change between systole and diastole, as shown by *in vivo*, *in situ*, and *ex vivo* experiments [12]. In healthy controls, E2A mobility was 45°, while in HCM hearts mobility was 23° [12]. Therefore, HCM sheetlets appear “stuck” in a systolic orientation, and unable to reorient to a diastolic confirmation (**Error! Reference source not found.**). As such, HCM hearts have a normal E2A during systole, but an abnormal E2A during diastole [12], [92]. Abnormal sheetlet orientation and mobility in HCM patients is thought to be due to their calcium sensitivity, and residual tension in the diastolic state [13].

In dilated cardiomyopathy (DCM) the ventricular lumen dilates, impairing ejection of blood, with patients progressing to heart failure with reduced ejection fraction. In DCM patients, E2A mobility is lower (20°) as compared with healthy controls (45°) [12]. In DCM hearts, sheetlets are “stuck” in a diastolic orientation, and unable to reorient to a systolic confirmation. This is supported by the E2A frequency distributions in diastole and systole, with DCM hearts showing a normal E2A distribution in diastole, but not systole.

Duchenne Muscular Dystrophy is a disease caused by a mutation in the gene that codes for dystrophin. It is characterized by muscle weakness, with death occurring due to respiratory failure or heart failure. Using the *Mdx* model of DMD, hearts were arrested in either systole or diastole, and perfused with either normal or low levels of calcium [27]. Under normal calcium conditions, *Mdx* mice showed reduced diastolic E2A, and reduced E2A mobility. Perfusion with a low concentration of calcium restored E2A mobility to normal levels, suggesting that calcium dynamics are an important component of sheetlet mechanics.

First Author	Year	Methods	Animal	Sample Size	Key Finding	Reference
Ferreira	2014	DTI *in vivo*	Human	22	HCM patients show systolic-like E2A during diastole.	[13]
Le	2020	DTI ex *vivo*	Sheep	6	Both helix angle and E2A are similar between term and preterm hearts.	[103]
Garcia-Canadilla	2019	HREM	Mice	56	HCM mice showed a loss of linear helix angle profile, fewer circumferential aggregate cardiomyocytes, and greater disarray during fetal development.	[44]
Cheng	2012	DTI and histology	Mice	27	Calcium mishandling is implicated in impaired sheetlet mechanics.	[104]
Carruth	2020	DTI and histology	Rat	16	In pressure-overload hypertrophy, sheetlet dispersion is greater in the subendocardium.	[61]
Das	2021	DTI *in vivo*	Human	30	Infarction reduces FA and E2A. Both measures were associated with reduced ejection fraction.	[105]

Table 3: *A summary of studies that have examined mesofunction in different cardiac pathologies.*

6. *In vivo* Assessment of Myocardial Mesostructure

There are several current and emerging methods for assessment of cardiac mesostructure *in vivo.* Key considerations for clinical translation include: motion compensation (Section 6.1), and the potential of combination diffusion-strain techniques for measuring mesostructural mechanics (Section 6.2).

6.1. Motion Compensation of *in vivo* cardiac DTI

Diffusion tensor MRI has provided substantial insight to the microstructural organization of tissues by enabling measurement of the diffusion coefficient of water along many directions. Probing the self-diffusion of water requires the use of strong gradient waveforms that also incur high sensitivity and data corruption form bulk tissue motion. For many *in vivo* applications the bulk motion can be controlled or mitigated (e.g. brain or prostate imaging), but the continuous motion of the heart presents a special challenge. Cardiac DTI requires at least four kinds of coincident motion compensation: patient compliance, respiratory management, ECG synchronization, and specialized diffusion encoding methods. Bulk motion of the heart that is not mitigated or accounted for can produce MRI signal phase accrual artefacts, and significant loss of signal. Minimizing motion during the MRI acquisition can be achieved by using fast single-shot echo-planar imaging readouts and navigator-gated or breath hold approaches to minimize respiratory motion [106]. Navigator-based approaches can be used to track motion, which allows for slice-tracking and increases acquisition efficiency [107].

Some cardiac DTI acquisition methods (e.g. stimulated echo-acquisition mode) align the image acquisition times with diastole, which is typically less dynamic than systole [108],

[109]. This approach requires longer scan times and has inherently lower SNR, but can be quite motion robust. Other approaches (e.g. motion compensated spin echo – echo planar imaging, SE-EPI) demonstrate robust data acquisition during end-systole, a time point that is highly repeatable and for which motion paths are very consistent.

The motion of spins through a magnetic field can be expressed with a Taylor series expansion (e.g. position, velocity, acceleration, etc.), and phase artifacts from high order motion features can be mitigated by adding additional diffusion sensitizing gradient waveforms that null the effects of non-stationary tissue. For example, M_1+M_2-nulled (i.e. velocity and acceleration nulled) DTI enables *in vivo* cardiac DTI with high signal-to-noise ratio, and SE-EPI can allow human *in vivo* cardiac DTI acquisitions of approximately 10 minutes for a single slice using SE-EPI [14][110]. M_2-nulling has been found to optimize the combination of b-value, signal-to-noise and insensitivity to motion [111].

6.2. DTI and Strain

One promising application of *in vivo* cardiac DTI is that it can be combined with strain imaging techniques (such as DENSE). The combination of cardiac DTI with strain imaging allows for the measurement of cardiac meso-function *in vivo* [10], [14], [15], [112]. The cardiac DTI acquisition measures the aggregate cardiomyocyte direction, and strain imaging method measures the displacement of pixels during the cardiac cycle. These mesostructural and functional data can be combined using various computational modeling approaches [10], [11], [14], [15], [112]. By measuring the displacement during the cardiac cycle along the aggregate cardiomyocyte direction, the aggregate cardiomyocyte strain can be calculated, as well as the reorientation of

aggregate cardiomyocyte helix angle through the cardiac cycle (**Error! Reference source not found.**). Unlike circumferential strain that varies according to transmural location, measurement of aggregate cardiomyocyte strain *in vivo* has been shown to be uniform across the wall [14]. Although these methods have so far been applied only to healthy humans, measurement of aggregate cardiomyocyte strain has the potential to identify cardiac pathology at the mesoscale, which could be masked by compensatory remodeling at the organ level.

7. Future Research and Conclusion

7.1. Future Work

The field of cardiac mesostructure is well positioned for new insights and developments. There is still some disagreement as to whether multiple sheetlet orientations are the norm throughout the heart. Future work along these lines would examine myocardial samples with multiple imaging modalities, and perhaps investigate the histology preparation parameters that most impact the presence or absence of multiple sheetlet populations in histology slides. The rearrangement of sheetlets during myocardial deformation would also benefit from mesostructural imaging of the same myocardial sample in multiple strain configurations, ideally *in vivo* or *in vitro*. Developments in cDTI pulse sequences, particularly improvements that reduce acquisition times and increase signal-to-noise ratio would be of high value, as scan length is currently a major impediment to their adoption in the clinic. A database of sheetlet orientations from different animal species and in different contraction states would be of great interest to the computational modelling field. In particular, mesostructural data from various disease models would be particularly valuable and would provide insights to the mesostructural features that translational researchers should investigate in human pathophysiology.

7.2. Conclusion

Developments in both *in vivo* and *ex vivo* imaging techniques allow for examination of cardiac mesostructure in unprecedented detail over the whole heart. Multiple studies have confirmed the critical contributions of sheetlets to ventricular wall thickening during the cardiac cycle. Impaired sheetlet mobility resulting from collagen deposition between

sheetlets and dysfunctional calcium handling may provide avenues for pharmacological treatment of impaired meso-function. Emerging approaches to combine meso-structural and meso-functional imaging techniques allow for the measurement of aggregate cardiomyocyte strain and sheetlet mobility, thereby providing mechanistic insight to cardiac function and dysfunction.

Acknowledgements

We thank Amy Thomas and Rudilyn Joyce Wilson for their assistance with preparing figures.

Grants

This work was supported, in part, by funding from the American Heart Association (AHA 19IPLOI34760294 to DBE), and the National Institutes of Health, National Heart, Lung, and Blood Institute (NIH/NHLBI R01-HL131823 to DBE, R01-HL152256 to DBE).

Disclosures

No conflicts of interest, financial or otherwise, are declared by the author(s).

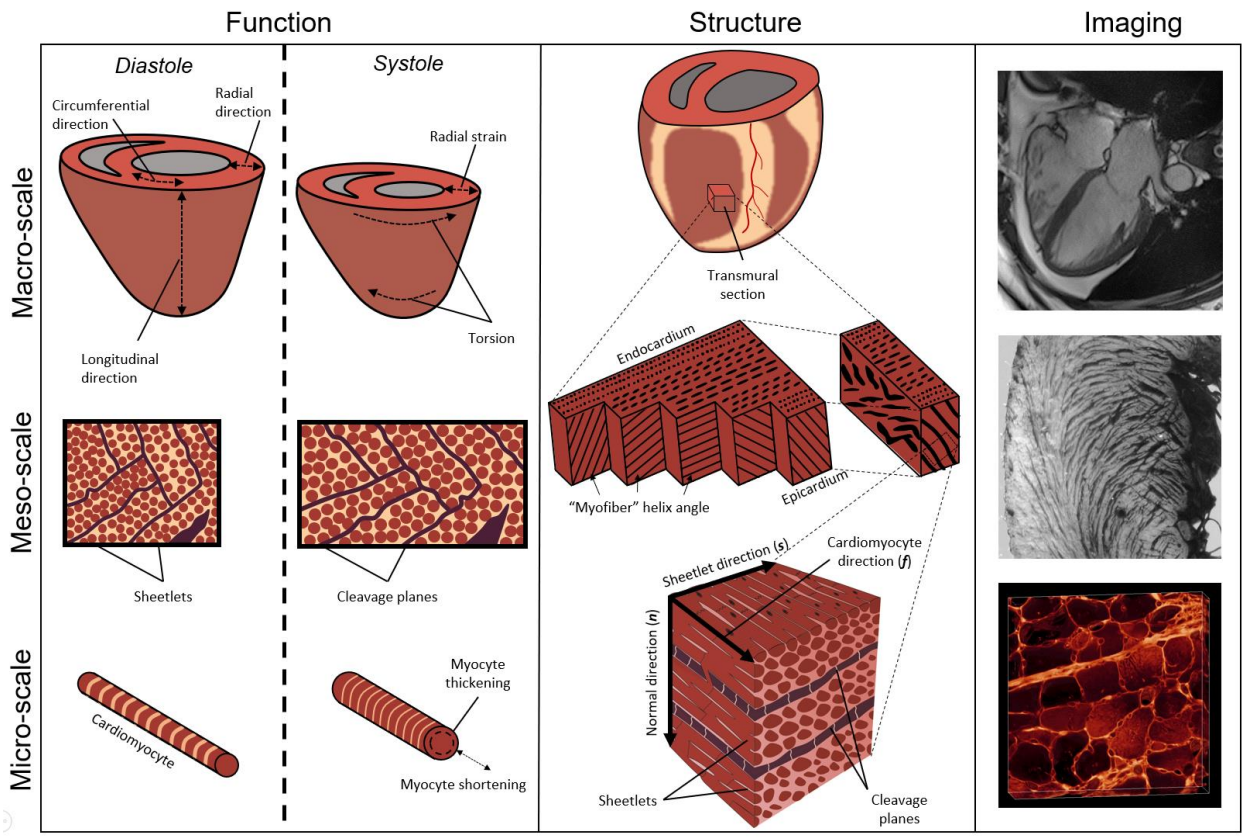

*Figure 1: The multi-scale structure and function of the cardiac ventricles. The mechanical function (left column) of the whole heart (top row) includes ejection fraction, torsion, radial, circumferential and longitudinal strains. At the meso-scale (middle row) mesofunction (middle left) includes transmural shear due to helix angle slope, helix angle reorientation during contraction, and sliding of sheetlets producing wall thickening. At the cellular level (bottom row), cardiomyocyte function (bottom left) includes both cellular shortening and transverse thickening. Myocardial mesostructure (center) shows a transmural block of myocardium with changing helix angle through the wall, as well as the right block showing cleavage planes giving rise to sheetlets. Microscale structure (bottom middle) shows cardiomyocytes with a cardiomyocyte longitudinal direction (**f**), which are bundled into sheetlets forming a plane along the both sheetlet (**s**) and **f***

*directions. Orthogonal to the sheetlet plane is the sheetlet-normal direction (**n**). The right column shows real imaging data including a four-chamber cardiac MRI (top right), a short-axis macrograph showing sheetlet structures across the left ventricular wall (middle right) and cardiomyocyte cross-sections and their organization into sheetlets (bottom right) using extended volume confocal microscopy.*

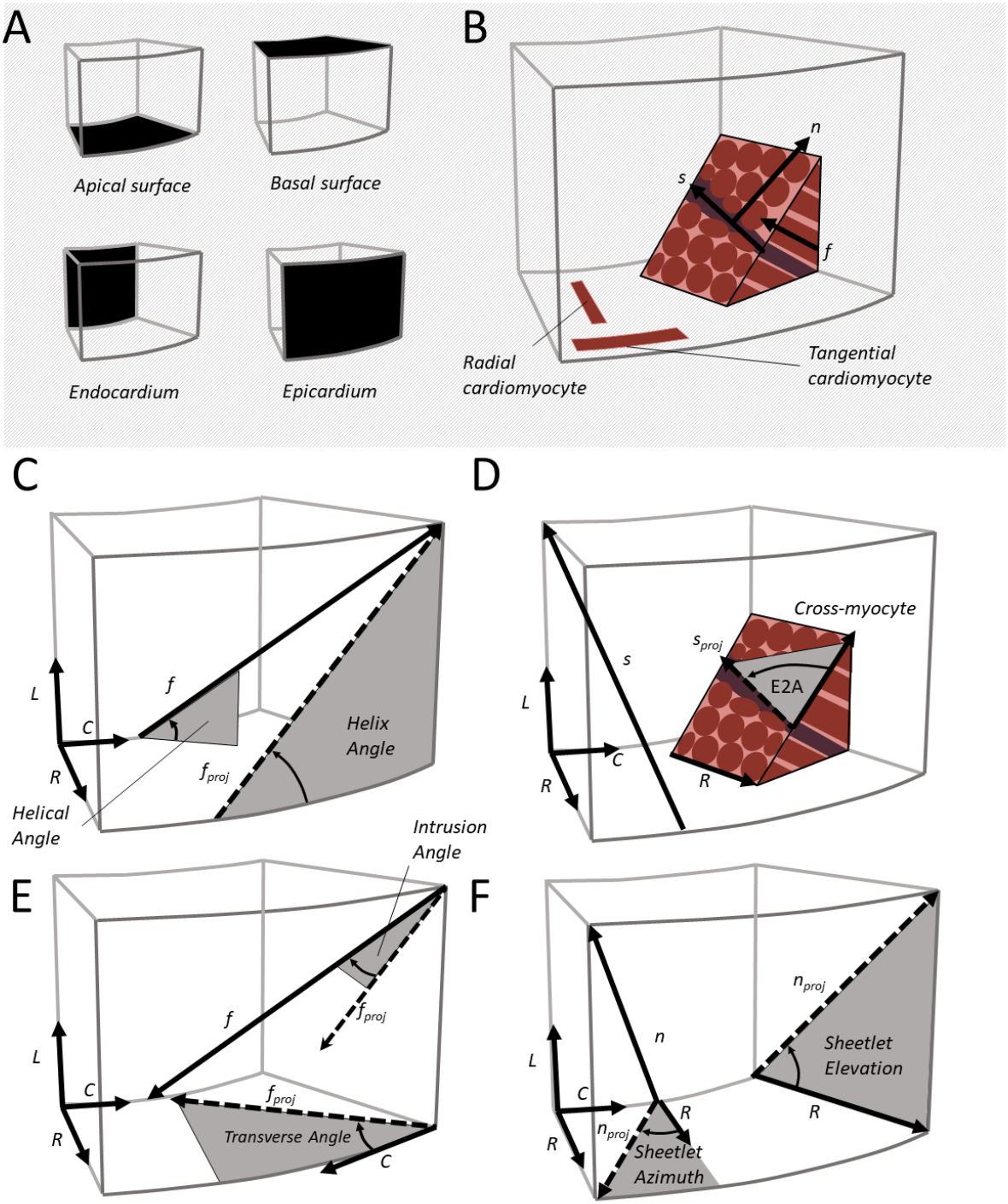

813

814 *Figure 2 Mesostructural co-ordinates and angles. The myocardium can be defined by*

815 *three orthogonal directions (top right), the aggregate cardiomyocyte (**f**), sheetlet (**s**) and*

816 *sheetlet-normal (**n**) directions. Helix angle (C) is the projection of the **f** onto the*

longitudinal-circumferential plane. E2A (D) is the projection of the sheetlet direction ***s*** *onto the cross-myocyte plane. The transverse angle (E) is the projection of* ***f*** *onto the short axis plane (radial-circumferential plane). Sheetlet elevation and sheetlet azimuth (F) are projections of the* ***n*** *onto the longitudinal-radial plane and the short-axis plane, respectively.*

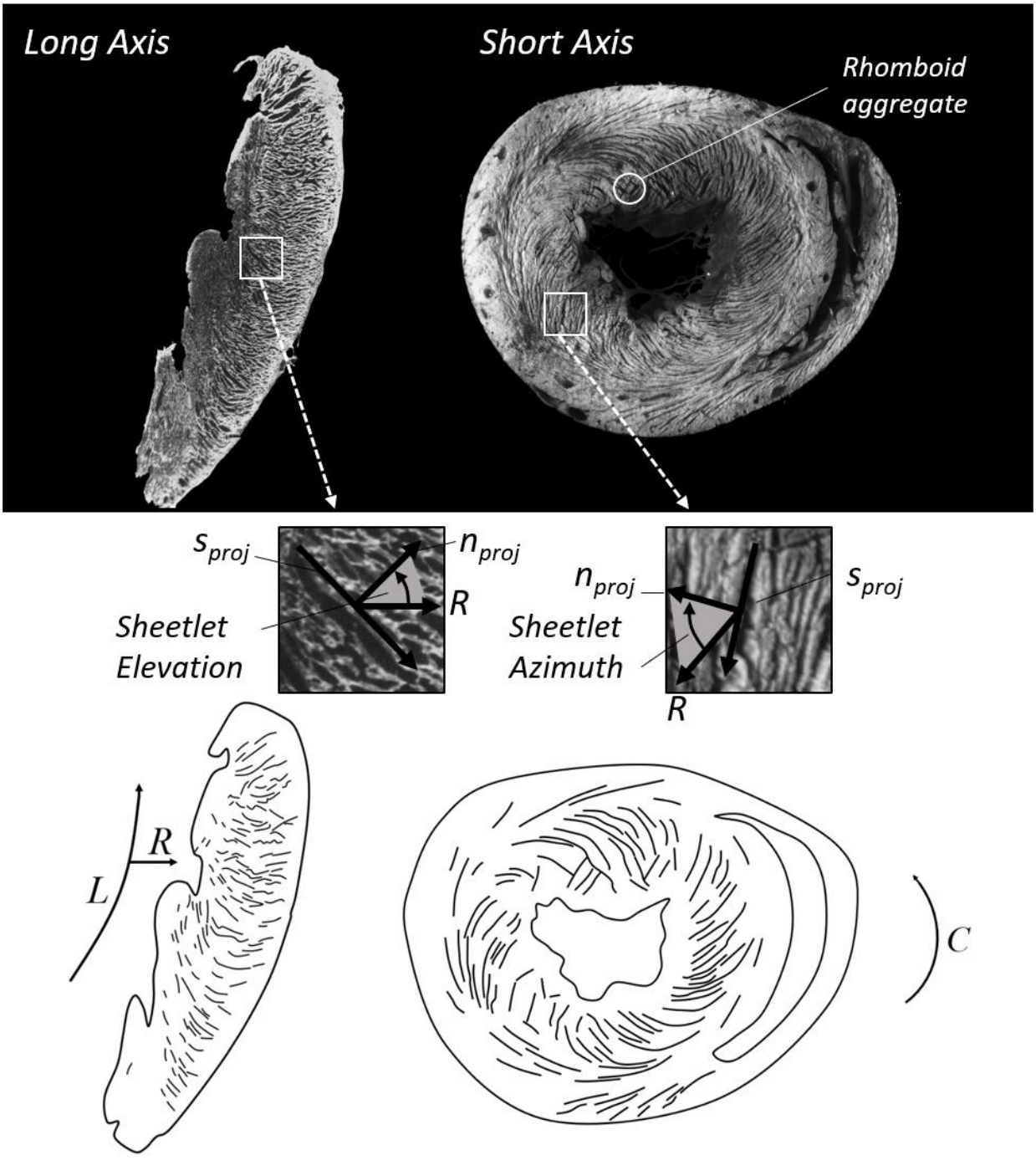

822

823 *Figure 3: Sheetlet structures imaged in cardiac long-axis (left) and short-axis (right)*

824 *views. The macrographs (top) show light myocardium with dark cleavage planes, and*

825 *schematic representations are also presented (bottom). Sheetlet elevation (middle left)*

826 *is shown as the angle between the radial direction (R) and the projection of the sheetlet-*

normal direction (n_{proj}) on the long-axis plane. Sheetlet azimuth (middle right) is shown as the angle between R and n_{proj} on the short-axis plane. The long-axis view shows cleavage planes extending in a radial pattern towards the epicardium, with local connections as opposed to a full transmural span. In the short-axis view, cleavage planes have a herringbone or V-shaped structure, with structural discontinuities located approximately in the mid-wall. Intersecting populations of sheetlets are most visible in the subendocardial surface of the short-axis micrograph (top right).

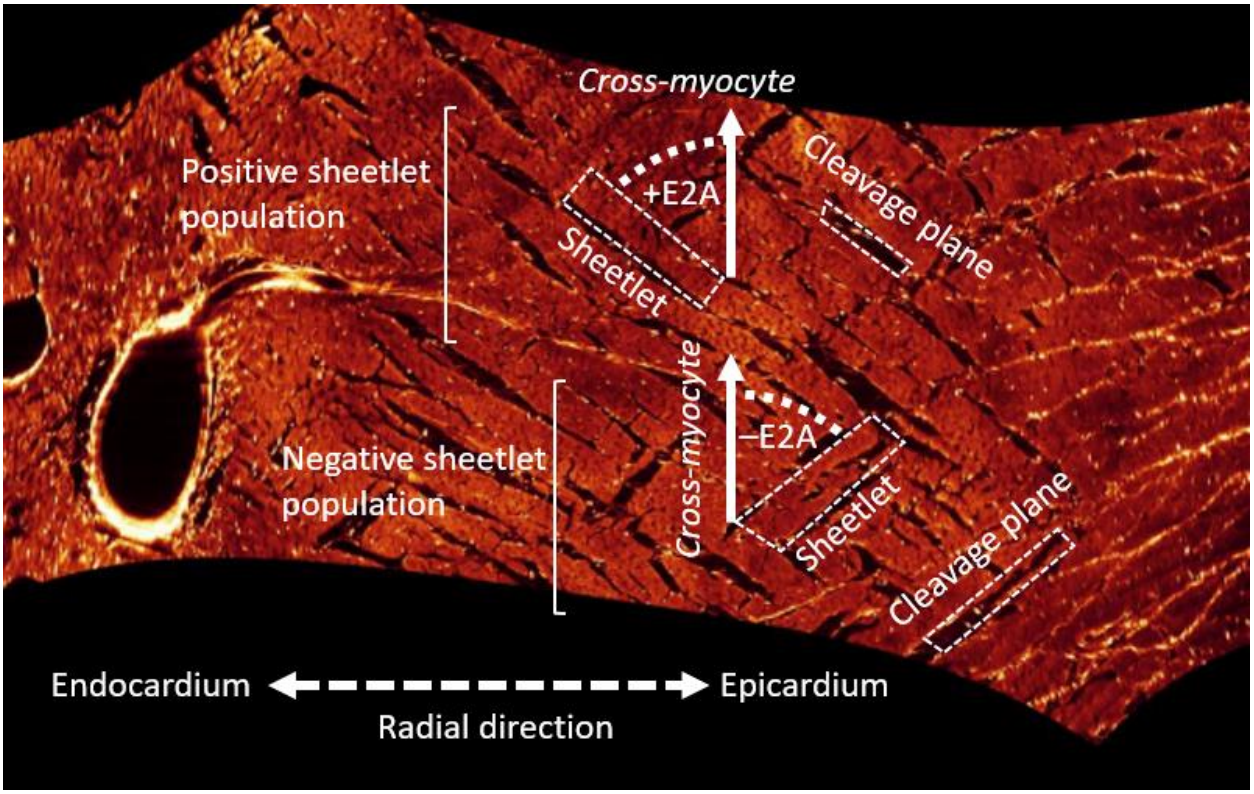

Figure 4: Orthogonal sheetlet populations. Imaging of the myocardium using extended volume confocal microscopy allows for a virtual cut that shows the cross-myocyte plane at all locations. In the mid-wall, two populations of sheetlets are revealed, one with a positive sheetlet angle (+E2A), and one with a negative sheetlet angle (–E2A).

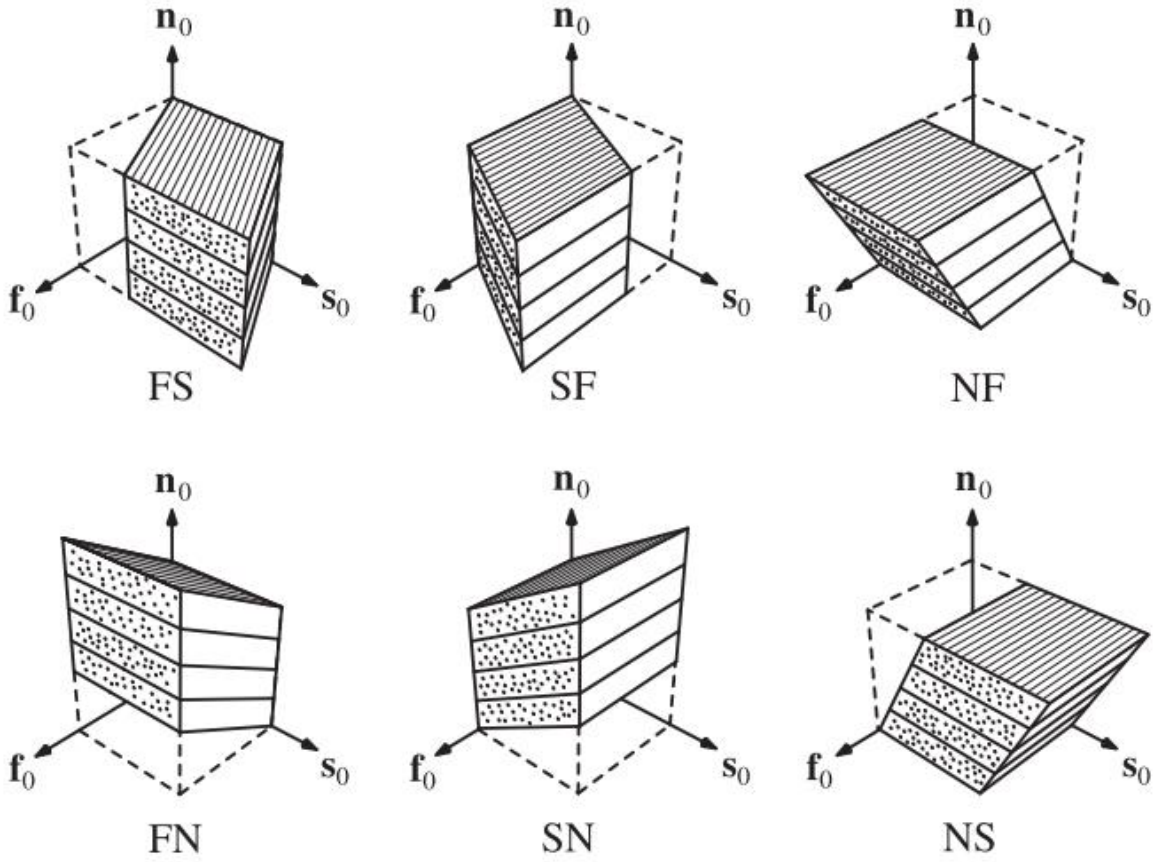

840

841 *Figure 5: Six modes of mesoscale shear strain. From an initial cube state, shear*
842 *deformation in the form of myocyte-sheet (FS), sheet-myocyte (SF), normal-myocyte*
843 *(NF), myocyte-sheet (FN), sheet-normal (SN) and normal-sheet (NS) modes are*
844 *applied. Due to the laminar mesostructure of the myocardium, the different shear modes*
845 *result in different shear stiffness measurements. In particular, the NF and NS shear*
846 *modes have reduced shear stiffness compared with the FS, FN, SF and SN modes.*
847 *This provides evidence that sliding of sheetlets facilitates myocardial deformation.*
848 *Reproduced with permission from Sommer et al. (2015)* [89].

849

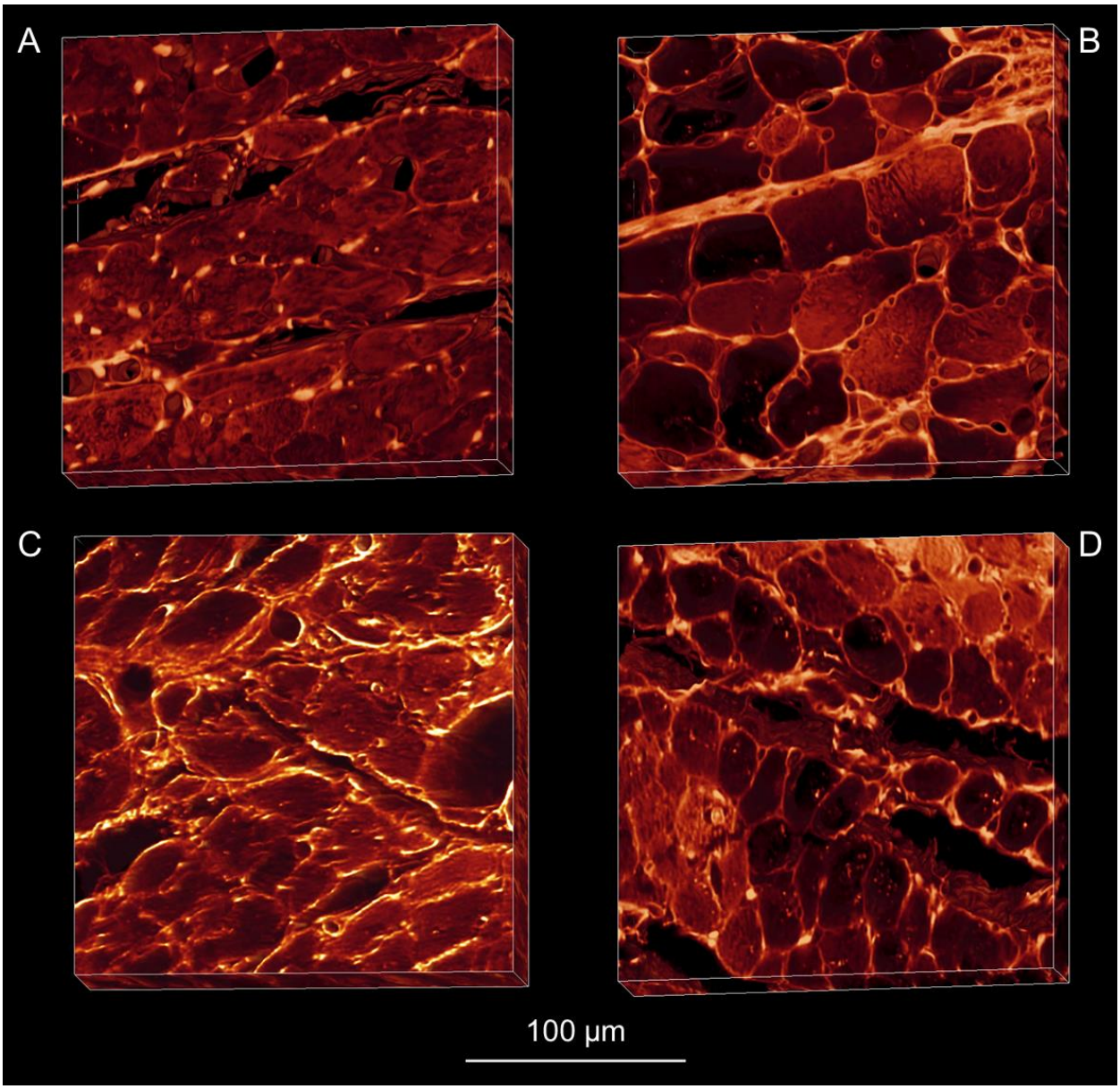

Figure 6: Extended volume confocal microscopy of laminar mesostructure in healthy (a), diseased (b) and treated (c, d) hearts. Sheetlets of the Wistar Kyoto (a) and treated spontaneously hypertensive rats (SHR, c, d) showed no collagen deposition between sheetlets, maintaining normal sheetlet organization. However SHR (b) myocardium showed marked deposition of collagen between sheetlets, and the loss of structural separation. Reproduced with permission from Wilson et al. (2020) [78].

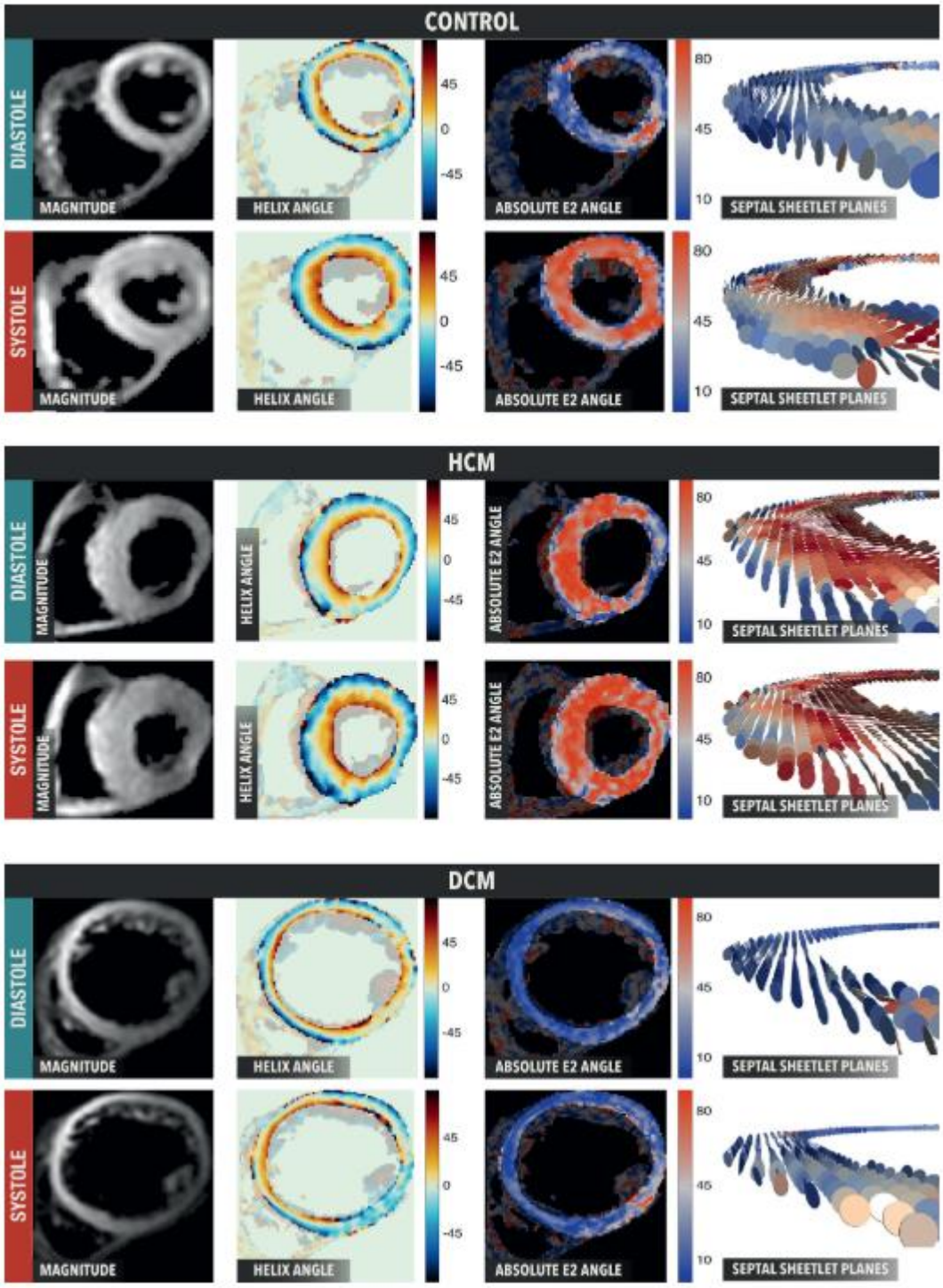

857

858 *Figure 7:* In vivo *sheetlet orientation in control, hypertrophic cardiomyopathy (HCM) and*

859 *dilated cardiomyopathy (DCM) hearts. In control hearts, E2A is low (blue) in diastole*

860 *and high (red) in systole. HCM hearts show high (red) E2A in both systole and diastole,*

while DCM hearts show low (blue) E2A in both systole and diastole. Reproduced under CC BY-NC-ND 4.0 from Nielles-vallespin et al. (2017) [57].

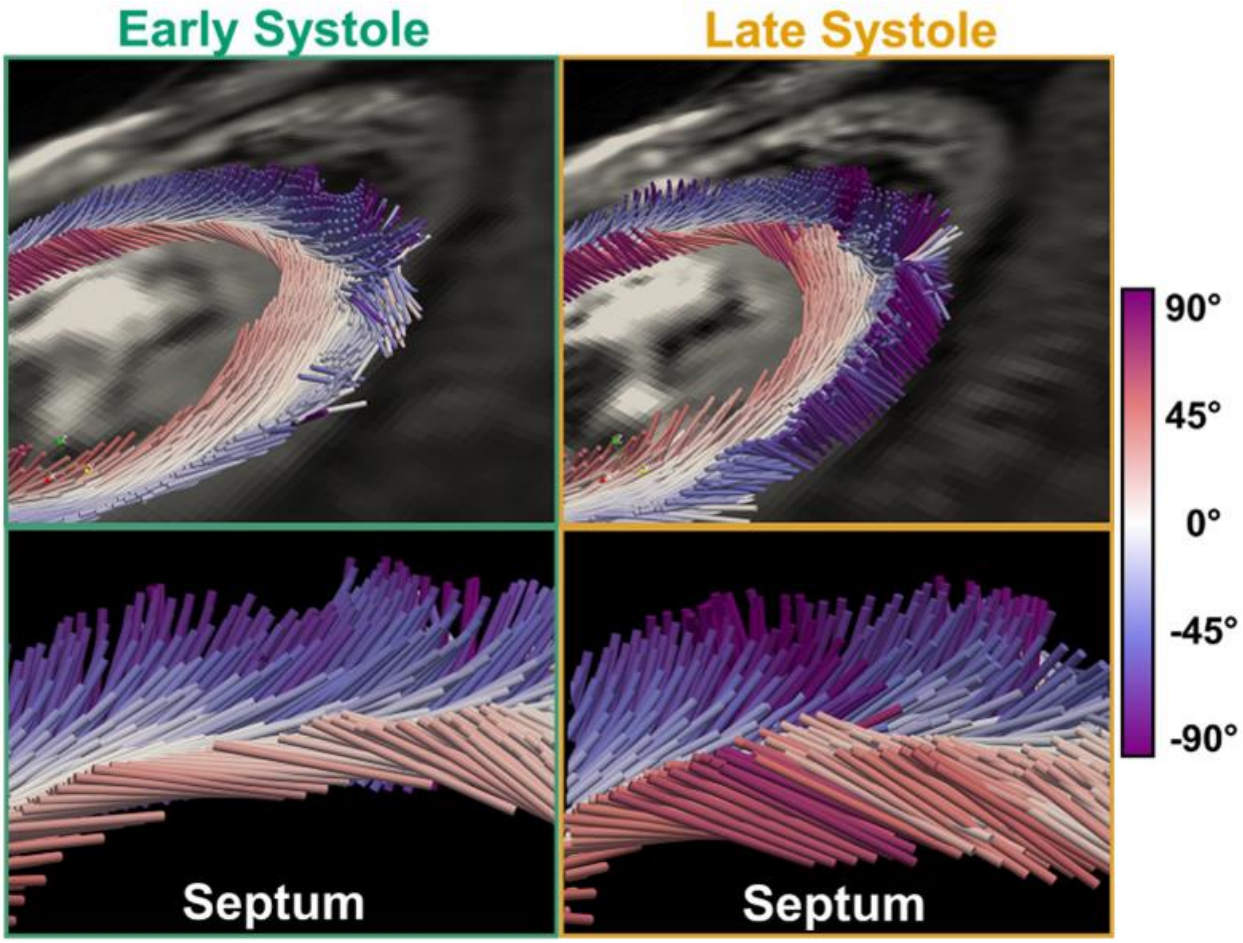

Figure 8: The reorientation of aggregate cardiomyocytes through the cardiac cycle. Cylinders represent the aggregate cardiomyocyte direction, with color indicating the helix angle. During early systole (left) to late systole (mid) subendocardial helix angle increases. Reproduced under CC BY 4.0 from Moulin et al. (2020) [15].

References

[1] H. M. Spotnitz, W. D. Spotnitz, T. S. Cottrell, D. Spiro, and E. H. Sonnenblick, "Cellular Basis for Volume Related Wall Thickness Changes in the Rat Left Ventricle," *J. Mol. Cell. Cardiol.*, vol. 6, pp. 317–331, 1974.

[2] R. P. Grant, "Notes on the Muscular Architecture of the Left Ventricle," *Circulation*, vol. 32, no. 2, 1965, doi: 10.1161/01.CIR.32.2.301.

[3] J. Auchampach *et al.*, "Measuring cardiomyocyte cell-cycle activity and proliferation in the age of heart regeneration," *Am. J. Physiol. Circ. Physiol.*, vol. 322, no. 4, pp. H579–H596, 2022, doi: 10.1152/ajpheart.00666.2021.

[4] M. Rienks, A. P. Papageorgiou, N. G. Frangogiannis, and S. Heymans, "Myocardial extracellular matrix: An ever-changing and diverse entity," *Circ. Res.*, vol. 114, no. 5, pp. 872–888, 2014, doi: 10.1161/CIRCRESAHA.114.302533.

[5] A. J. Pope *et al.*, "Three-dimensional transmural organization of perimysial collagen in the heart," *Am. J. Physiol. - Hear. Circ. Physiol.*, vol. 295, pp. 1243–1252, 2008, doi: 10.1152/ajpheart.00484.2008.

[6] K. Howe, J. M. Ross, D. S. Loiselle, J. C. Han, and D. J. Crossman, "Right-sided heart failure is also associated with transverse tubule remodeling in the left ventricle," *Am. J. Physiol. - Hear. Circ. Physiol.*, vol. 321, no. 5, pp. H940–H947, 2021, doi: 10.1152/ajpheart.00298.2021.

[7] M. L. Trew *et al.*, "Cardiac electrophysiology and tissue structure : bridging the scale gap with a joint measurement and modelling paradigm," *Exp. Physiol.*, vol.

91, no. 2, pp. 355–370, 2006, doi: 10.1113/expphysiol.2005.031054.

[8] J. Rodriguez Padilla *et al.*, “Impact of Intraventricular Septal Fiber Orientation on Cardiac Electromechanical Function,” *Am. J. Physiol. Circ. Physiol.*, no. March, 2022, doi: 10.1152/ajpheart.00050.2022.

[9] N. T. Olsen, C. Goransson, N. Vejlstrup, and J. Carlsen, “Myocardial adaptation and exercise performance in patients with pulmonary arterial hypertension assessed with patient-specific computer simulations,” *Am. J. Physiol. - Hear. Circ. Physiol.*, vol. 321, no. 5, pp. H865–H880, 2021, doi: 10.1152/ajpheart.00442.2021.

[10] I. A. Verzhbinsky, L. E. Perotti, K. Moulin, T. E. Cork, M. Loecher, and D. B. Ennis, “Estimating Aggregate Cardiomyocyte Strain Using In Vivo Diffusion and Displacement Encoded MRI,” *IEEE Trans. Med. Imaging*, vol. 39, no. 3, pp. 656–667, 2020.

[11] C. Von Deuster *et al.*, “Studying Dynamic Myofiber Aggregate Reorientation in Dilated Cardiomyopathy Using in Vivo Magnetic Resonance Diffusion Tensor Imaging,” *Circ. Cardiovasc. Imaging*, vol. 9, no. 10, pp. 1–10, 2016, doi: 10.1161/CIRCIMAGING.116.005018.

[12] S. Nielles-vallespin *et al.*, “Assessment of Myocardial Microstructural Dynamics by In Vivo Diffusion Tensor Cardiac Magnetic Resonance,” *J. Am. Coll. Cardiol.*, vol. 69, no. 6, 2017, doi: 10.1016/j.jacc.2016.11.051.

[13] P. F. Ferreira *et al.*, “In vivo cardiovascular magnetic resonance diffusion tensor imaging shows evidence of abnormal myocardial laminar orientations and mobility

in hypertrophic cardiomyopathy," *J. Cardiovasc. Magn. Reson.*, vol. 16, no. 1, p. 87, 2014.

[14] K. Moulin, P. Croisille, M. Viallon, I. A. Verzhbinsky, L. E. Perotti, and D. B. Ennis, "Myofiber strain in healthy humans using DENSE and cDTI," *Magn. Reson. Med.*, vol. 86, no. 1, pp. 277–292, 2021, doi: 10.1002/mrm.28724.

[15] K. Moulin, I. A. Verzhbinsky, N. G. Maforo, L. E. Perotti, and D. B. Ennis, "Probing cardiomyocyte mobility with multiphase cardiac diffusion tensor MRI," *PLoS One*, vol. 15, no. 11 November, 2020, doi: 10.1371/journal.pone.0241996.

[16] S. H. Gilbert, A. P. Benson, P. Li, and A. V. Holden, "Regional localisation of left ventricular sheet structure: integration with current models of cardiac fibre, sheet and band structure," *Eur. J. Cardio-thoracic Surg.*, vol. 32, no. 2, pp. 231–249, 2007, doi: 10.1016/j.ejcts.2007.03.032.

[17] R. H. Anderson, P. F. Niederer, D. Sanchez-Quintana, R. S. Stephenson, and P. Agger, "How are the cardiomyocytes aggregated together within the walls of the left ventricular cone?," *J. Anat.*, vol. 235, no. 4, pp. 697–705, 2019, doi: 10.1111/joa.13027.

[18] T. Arts, K. D. Costa, J. W. Covell, and A. D. McCulloch, "Relating myocardial laminar architecture to shear strain and muscle fiber orientation," *Am. J. Physiol. - Hear. Circ. Physiol.*, vol. 280, no. 5 49-5, 2001, doi: 10.1152/ajpheart.2001.280.5.h2222.

[19] S. Dokos, B. H. Smaill, A. A. Young, and I. J. LeGrice, "Shear properties of passive ventricular myocardium," *Am. J. Physiol. - Hear. Circ. Physiol.*, vol. 283,

no. 6 52-6, pp. 2650–2659, 2002, doi: 10.1152/ajpheart.00111.2002.

[20] K. D. Costa, Y. Takayama, A. D. McCulloch, and J. W. Covell, “Laminar fiber architecture and three-dimensional systolic mechanics in canine ventricular myocardium,” *Am. J. Physiol. - Hear. Circ. Physiol.*, vol. 276, no. 2 45-2, 1999, doi: 10.1152/ajpheart.1999.276.2.h595.

[21] I. J. Legrice *et al.*, “Progression of myocardial remodeling and mechanical dysfunction in the spontaneously hypertensive rat Progression of myocardial remodeling and mechanical dysfunction in the spontaneously hypertensive rat,” *Am. J. Physiol. - Hear. Circ. Physiol.*, vol. 303, pp. H1353–H1365, 2012, doi: 10.1152/ajpheart.00748.2011.

[22] I. J. LeGrice, P. J. Hunter, and B. H. Smaill, “Laminar structure of the heart : a mathematical model,” *Am. J. Physiol. - Hear. Circ. Physiol.*, vol. 272, pp. H2466–H2476, 1997.

[23] S. H. Gilbert *et al.*, “Visualization and quantification of whole rat heart laminar structure using high-spatial resolution contrast-enhanced MRI,” *Am. J. Physiol. - Hear. Circ. Physiol.*, vol. 302, no. 1, pp. H287–H298, 2012, doi: 10.1152/ajpheart.00824.2011.

[24] I. J. LeGrice, B. H. Smaill, L. Chai, S. G. Edgar, B. Gavin, and P. J. Hunter, “Laminar structure of the heart: ventricular myocyte arrangement and connective tissue architecture in the dog,” *Am J Physiol Hear. Circ Physiol*, vol. 260, pp. H1365–1378., 1995, doi: 10.1152/ajpheart.1995.269.2.h571.

[25] J. Chen *et al.*, “Regional ventricular wall thickening reflects changes in cardiac

fiber and sheet structure during contraction: Quantification with diffusion tensor MRI," *Am. J. Physiol. - Hear. Circ. Physiol.*, vol. 289, no. 5 58-5, pp. 1898–1907, 2005, doi: 10.1152/ajpheart.00041.2005.

[26] H. Ashikaga, J. C. Criscione, J. H. Omens, J. W. Covell, and N. B. Ingels, "Transmural left ventricular mechanics underlying torsional recoil during relaxation," *Am. J. Physiol. Circ. Physiol.*, vol. 286, no. 2, pp. H640–H647, 2004, doi: 10.1152/ajpheart.00575.2003.

[27] Y.-J. J. Cheng, D. Lang, S. D. Caruthers, I. R. Efimov, J. Chen, and S. A. Wickline, "Focal but reversible diastolic sheet dysfunction reflects regional calcium mishandling in dystrophic mdx mouse hearts," *Am. J. Physiol. Circ. Physiol.*, vol. 303, no. 5, pp. H559–H568, 2012, doi: 10.1152/ajpheart.00321.2012.

[28] H. Ashikaga, J. W. Covell, and J. H. Omens, "Diastolic dysfunction in volume-overload hypertrophy is associated with abnormal shearing of myolaminar sheets," *Am. J. Physiol. Circ. Physiol.*, vol. 288, no. 6, pp. H2603–H2610, 2005, doi: 10.1152/ajpheart.01276.2004.

[29] Y. Takayama, K. D. Costa, J. W. Covell, K. D. Costa, and W. James, "Contribution of laminar myofiber architecture to load-dependent changes in mechanics of LV myocardium," *Am. J. Physiol. Circ. Physiol.*, vol. 92093, no. 4, pp. 1510–1520, 2002.

[30] D. D. Streeter and D. L. Bassett, "An engineering analysis of myocardial fiber orientation in pig's left ventricle in systole," *Anat. Rec.*, vol. 155, no. 4, pp. 503–511, 1966.

[31] D. D. Streeter, “Gross morphology and fiber geometry of the heart,” in *Handbook of Physiology*, 1979, pp. 61–112.

[32] D. D. Streeter *et al.*, “Fiber orientation in the canine left ventricle during diastole and systole,” *Circ. Res.*, vol. 24, no. 3, pp. 339–347, 1969.

[33] E. A. Sallin, “Fiber orientation and ejection fraction in the human left ventricle.,” *Biophys. J.*, vol. 9, no. 7, pp. 954–64, 1969, doi: 10.1016/S0006-3495(69)86429-5.

[34] N. B. Ingels, “Myocardial fiber architecture and left ventricular function,” *Technol. Heal. Care*, vol. 5, no. 1–2, pp. 45–52, 1997, doi: 10.3233/thc-1997-51-205.

[35] A. A. Young and B. R. Cowan, “Evaluation of left ventricular torsion by cardiovascular magnetic resonance,” *J. Cardiovasc. Magn. Reson.*, vol. 14, no. 49, pp. 1–10, 2012.

[36] M. Froeling, G. J. Strijkers, and P. R. Luijten, “Diffusion Tensor MRI of the Heart – In Vivo Imaging of Myocardial Fiber Architecture,” *Curr. Cardiovasc. Imaging Rep.*, vol. 7, 2014, doi: 10.1007/s12410-014-9276-y.

[37] H. Dejea *et al.*, “Comprehensive Analysis of Animal Models of Cardiovascular Disease using Multiscale X-Ray Phase Contrast Tomography,” *Sci. Rep.*, vol. 9, no. 1, pp. 1–12, 2019, doi: 10.1038/s41598-019-43407-z.

[38] A. Giannakidis and G. T. Gullberg, “Transmural Remodeling of Cardiac Microstructure in Aged Spontaneously Hypertensive Rats by Diffusion Tensor MRI,” *Front. Physiol.*, vol. 11, no. March, pp. 1–12, 2020, doi:

10.3389/fphys.2020.00265.

[39] I. Teh *et al.*, “Validation of diffusion tensor MRI measurements of cardiac microstructure with structure tensor synchrotron radiation imaging,” *J. Cardiovasc. Magn. Reson.*, vol. 19, no. 1, p. 31, 2017.

[40] P. Schmid *et al.*, “Statistical analysis of the angle of intrusion of porcine ventricular myocytes from epicardium to endocardium using diffusion tensor magnetic resonance imaging,” *Anat. Rec.*, vol. 290, no. 11, pp. 1413–1423, 2007, doi: 10.1002/ar.20604.

[41] P. P. Lunkenheimer *et al.*, “Three-dimensional architecture of the left ventricular myocardium,” *Anat. Rec. - Part A Discov. Mol. Cell. Evol. Biol.*, vol. 288, no. 6, pp. 565–578, 2006, doi: 10.1002/ar.a.20326.

[42] G. B. Sands, B. H. Smaill, and I. J. Legrice, “Virtual Sectioning of Cardiac Tissue Relative to Fiber Orientation,” in *30th Annual International IEEE EMBS Conference*, 2008, pp. 226–229, doi: 10.1109/IEMBS.2008.4649131.

[43] P. P. Lunkenheimer *et al.*, “The forces generated within the musculature of the left ventricular wall,” *Heart*, vol. 90, no. 2, pp. 200–207, 2004, doi: 10.1136/hrt.2003.011650.

[44] P. Garcia-Canadilla *et al.*, “Myoarchitectural disarray of hypertrophic cardiomyopathy begins pre-birth,” *J. Anat.*, vol. 235, no. 5, pp. 962–976, 2019, doi: 10.1111/joa.13058.

[45] A. A. Young, C. M. Kramer, V. A. Ferrari, L. Axel, and N. Reichek, “Three-

dimensional left ventricular deformation in hypertrophic cardiomyopathy," *Circulation*, vol. 90, no. 2, pp. 854–867, 1994.

[46] S. W. J. Ubbink, P. H. M. Bovendeerd, T. Delhaas, T. Arts, and F. N. van de Vosse, "Towards model-based analysis of cardiac MR tagging data: Relation between left ventricular shear strain and myofiber orientation," *Med. Image Anal.*, vol. 10, no. 4, pp. 632–641, 2006, doi: 10.1016/j.media.2006.04.001.

[47] P. Agger and R. S. Stephenson, "Assessing myocardial architecture: The challenges and controversies," *J. Cardiovasc. Dev. Dis.*, vol. 7, no. 4, pp. 1–17, 2020, doi: 10.3390/jcdd7040047.

[48] J. B. Caulfield and T. K. Borg, "The collagen network of the heart.," *Lab. Invest.*, vol. 40, no. 3, pp. 364–372, 1979.

[49] I. LeGrice, P. Hunter, A. Young, B. Smaill, and N. Zealand, "The architecture of the heart: A data-based model," *Philos. Trans. R. Soc. A Math. Phys. Eng. Sci.*, vol. 359, no. 1783, pp. 1217–1232, 2001, doi: 10.1098/rsta.2001.0827.

[50] I. Teh *et al.*, "Resolving Fine Cardiac Structures in Rats with High-Resolution Diffusion Tensor Imaging," *Sci. Rep.*, no. July, 2016, doi: 10.1038/srep30573.

[51] J. Magat *et al.*, "3D MRI of explanted sheep hearts with submillimeter isotropic spatial resolution: comparison between diffusion tensor and structure tensor imaging," *Magn. Reson. Mater. Physics, Biol. Med.*, no. 0123456789, 2021, doi: 10.1007/s10334-021-00913-4.

[52] O. M. Abdullah *et al.*, "Diffusion tensor imaging and histology of developing

hearts,” *NMR Biomed.*, vol. 29, no. 10, pp. 1338–1349, 2016, doi: 10.1002/nbm.3576.

[53] P. W. Hales, J. E. Schneider, R. A. B. B. Burton, B. J. Wright, C. Bollensdorff, and P. Kohl, “Histo-anatomical structure of the living isolated rat heart in two contraction states assessed by diffusion tensor MRI,” *Prog. Biophys. Mol. Biol.*, vol. 110, no. 2–3, pp. 319–330, 2012, doi: 10.1016/j.pbiomolbio.2012.07.014.

[54] G. B. Sands, D. A. Gerneke, D. A. Hooks, C. R. Green, B. H. Smaill, and I. A. N. J. Legrice, “Automated imaging of extended tissue volumes using confocal microscopy,” *Microsc. Res. Tech.*, vol. 67, no. 5, pp. 227–239, 2005, doi: 10.1002/jemt.20200.

[55] S. Wang, F. Varray, W. Liu, P. Clarysse, and I. E. Magnin, “Measurement of local orientation of cardiomyocyte aggregates in human left ventricle free wall samples using X-ray phase-contrast microtomography,” *Med. Image Anal.*, 2021, doi: 10.1016/j.media.2021.102269.

[56] P. Helm, M. F. Beg, M. I. Miller, R. L. Winslow, and L. Raimond, “Measuring and mapping cardiac fiber and laminar architecture using diffusion tensor MR imaging,” *Ann. N. Y. Acad. Sci.*, vol. 1047, no. 1, pp. 296–307, 2005.

[57] O. Bernus *et al.*, “Comparison of diffusion tensor imaging by cardiovascular magnetic resonance and gadolinium enhanced 3D image intensity approaches to investigation of structural anisotropy in explanted rat hearts,” *J. Cardiovasc. Magn. Reson.*, vol. 17, no. 1, pp. 1–27, 2015, doi: 10.1186/s12968-015-0129-x.

[58] G. Kung *et al.*, “The presence of two local myocardial sheet populations confirmed

by diffusion tensor MRI and histological validation," *J Magn Reson Imaging*, vol. 34, no. 5, pp. 1080–1091, 2011, doi: 10.1002/jmri.22725.

[59] S. Angeli, N. Befera, J.-M. Peyrat, E. Calabrese, G. A. Johnson, and C. Constantinides, "A high-resolution cardiovascular magnetic resonance diffusion tensor map from ex-vivo C57BL/6 murine hearts," *J. Cardiovasc. Magn. Reson.*, vol. 16, no. 1, p. 77, 2014.

[60] K. Haliot *et al.*, "3D High Resolution Imaging of Human Heart for Visualization of the Cardiac Structure," *Int. Conf. Funct. Imaging Model. Hear.*, pp. 196–207, 2019.

[61] E. D. Carruth, I. Teh, J. E. Schneider, A. D. McCulloch, J. H. Omens, and L. R. Frank, "Regional variations in ex-vivo diffusion tensor anisotropy are associated with cardiomyocyte remodeling in rats after left ventricular pressure overload," *J. Cardiovasc. Magn. Reson.*, vol. 22, no. 1, pp. 1–13, 2020, doi: 10.1186/s12968-020-00615-1.

[62] G. D. Buckberg *et al.*, "Left Ventricular Form and Function," *Circulation*, vol. 110, no. 14, pp. 1–4, 2004, doi: 10.1161/01.cir.0000143625.56882.5c.

[63] S. Nielles-vallespin, A. Scott, P. Ferreira, Z. Khalique, D. Pennell, and D. Firmin, "Cardiac Diffusion : Technique and Practical Applications," *J. Magn. Reson. Imaging*, vol. 52, no. 2, pp. 348–368, 2019, doi: 10.1002/jmri.26912.

[64] D. F. Scollan, A. Holmes, R. Winslow, and J. Forder, "Histological validation of myocardial microstructure obtained from diffusion tensor magnetic resonance imaging," *Am. J. Physiol. Circ. Physiol.*, vol. 275, no. 6, pp. H2308–H2318, 1998.

[65] A. A. Holmes, D. F. Scollan, and R. L. Winslow, “Direct histological validation of diffusion tensor MRI in formaldehyde-fixed myocardium,” *Magn. Reson. Med.*, vol. 44, no. 1, pp. 157–161, 2000, doi: 10.1002/1522-2594(200007)44:1<157::AID-MRM22>3.0.CO;2-F.

[66] E. W. Hsu, A. L. Muzikant, S. A. Matulevicius, R. C. Penland, and C. S. Henriquez, “Magnetic resonance myocardial fiber-orientation mapping with direct histological correlation,” *Am. J. Physiol. - Hear. Circ. Physiol.*, vol. 274, no. 5 43-5, pp. 1627–1634, 1998, doi: 10.1152/ajpheart.1998.274.5.h1627.

[67] P. A. Helm, H. J. Tseng, L. Younes, E. R. McVeigh, and R. L. Winslow, “Ex vivo 3D diffusion tensor imaging and quantification of cardiac laminar structure,” *Magn. Reson. Med.*, vol. 54, no. 4, pp. 850–859, 2005, doi: 10.1002/mrm.20622.

[68] W. I. Tseng, V. J. Wedeen, T. G. Reese, R. N. Smith, and E. F. Halpern, “Diffusion Tensor MRI of Myocardial Fibers and Sheets : Correspondence With Visible Cut-Face Texture,” *J. Magn. Reson. Imaging*, vol. 17, pp. 31–42, 2003, doi: 10.1002/jmri.10223.

[69] J. Chen *et al.*, “Remodeling of cardiac fiber structure after infarction in rats quantified with diffusion tensor MRI,” *Am. J. Physiol. - Hear. Circ. Physiol.*, vol. 285, no. 3 54-3, pp. 946–954, 2003, doi: 10.1152/ajpheart.00889.2002.

[70] G. L. Kung *et al.*, “Microstructural infarct border zone remodeling in the post-infarct swine heart measured by diffusion tensor MRI,” *Front. Physiol.*, vol. 9, no. AUG, pp. 1–9, 2018, doi: 10.3389/fphys.2018.00826.

[71] M. Reichardt, M. Töpperwien, A. Khan, F. Alves, and T. Salditt, “Fiber orientation

in a whole mouse heart reconstructed by laboratory phase-contrast micro-CT," *J. Med. Imaging*, vol. 7, no. 02, p. 1, 2020, doi: 10.1117/1.jmi.7.2.023501.

[72] F. Varray, I. Mirea, M. Langer, F. Peyrin, L. Fanton, and I. E. Magnin, "Extraction of the 3D local orientation of myocytes in human cardiac tissue using X-ray phase-contrast micro-tomography and multi-scale analysis," *Med. Image Anal.*, vol. 38, pp. 117–132, 2017, doi: 10.1016/j.media.2017.02.006.

[73] I. Soveral *et al.*, "Early cardiac remodeling in aortic coarctation: insights from fetal and neonatal functional and structural assessment," *Ultrasound Obstet. Gynecol.*, vol. 56, no. 6, pp. 837–849, 2020, doi: 10.1002/uog.21970.

[74] G. B. Sands *et al.*, "It's clearly the heart! Optical transparency, cardiac tissue imaging, and computer modelling," *Prog. Biophys. Mol. Biol.*, vol. 168, pp. 18–32, 2022, doi: 10.1016/j.pbiomolbio.2021.06.005.

[75] F. Giardini *et al.*, "Quantification of Myocyte Disarray in Human Cardiac Tissue," *Front. Physiol.*, vol. 12, no. November, pp. 1–14, 2021, doi: 10.3389/fphys.2021.750364.

[76] W. R. Goodyer *et al.*, "Transcriptomic profiling of the developing cardiac conduction system at single-cell resolution," *Circ. Res.*, vol. 125, no. 4, pp. 379–397, 2019, doi: 10.1161/CIRCRESAHA.118.314578.

[77] P. Fei *et al.*, "Cardiac Light-Sheet Fluorescent Microscopy for Multi-Scale and Rapid Imaging of Architecture and Function," *Sci. Rep.*, vol. 6, no. October 2015, pp. 1–12, 2016, doi: 10.1038/srep22489.

[78] A. J. Wilson *et al.*, “Myocardial Laminar Organization Is Retained in Angiotensin-Converting Enzyme Inhibitor Treated SHRs,” *Exp. Mech.*, vol. 61, no. 1, pp. 31–40, 2020, doi: 10.1007/s11340-020-00622-4.

[79] M. L. Milne, G. K. Singh, J. G. Miller, K. D. Wallace, and M. R. Holland, “Toward 3-D Echocardiographic Determination of Regional Myofiber Structure,” *Ultrasound Med. Biol.*, vol. 42, no. 2, pp. 607–618, 2016, doi: 10.1016/j.ultrasmedbio.2015.09.024.

[80] C. Papadacci *et al.*, “Imaging the dynamics of cardiac fiber orientation in vivo using 3D Ultrasound Backscatter Tensor Imaging,” *Sci. Rep.*, vol. 7, no. 1, pp. 1–9, 2017, doi: 10.1038/s41598-017-00946-7.

[81] W. N. Lee *et al.*, “Mapping myocardial fiber orientation using echocardiography-based shear wave imaging,” *IEEE Trans. Med. Imaging*, vol. 31, no. 3, pp. 554–562, 2012, doi: 10.1109/TMI.2011.2172690.

[82] C. J. Goergen *et al.*, “Optical coherence tractography using intrinsic contrast,” *Opt. Lett.*, vol. 37, no. 18, p. 3882, 2012, doi: 10.1364/ol.37.003882.

[83] C. Fan and G. Yao, “Imaging myocardial fiber orientation using polarization sensitive optical coherence tomography,” *Biomed. Opt. Express*, vol. 4, no. 3, p. 460, 2013, doi: 10.1364/boe.4.000460.

[84] Y. Wang, K. Zhang, N. B. Wasala, X. Yao, D. Duan, and G. Yao, “Histology validation of mapping depth-resolved cardiac fiber orientation in fresh mouse heart using optical polarization tractography,” *Biomed. Opt. Express*, vol. 5, no. 8, p. 2843, 2014, doi: 10.1364/boe.5.002843.

[85] L. K. Waldman, D. Nosan, F. Villarreal, and J. W. Covell, “Relation between transmural deformation and local myofiber direction in canine left ventricle,” *Circ. Res.*, vol. 63, no. 3, pp. 550–562, 1988.

[86] I. J. LeGrice, Y. Takayama, and J. W. Covell, “Transverse Shear Along Myocardial Cleavage Planes Provides a Mechanism for Normal Systolic Wall Thickening,” *Circ. Res.*, vol. 77, no. 1, pp. 182–193, 1995.

[87] C. Omann *et al.*, “Resolving the natural myocardial remodelling brought upon by cardiac contraction ; a porcine ex-vivo cardiovascular magnetic resonance study of the left and right ventricle,” *J. Cardiovasc. Magn. Reson.*, vol. 21, no. 35, pp. 1–19, 2019.

[88] K. B. Harrington *et al.*, “Direct measurement of transmural laminar architecture in the anterolateral wall of the ovine left ventricle : new implications for wall thickening mechanics,” *Am. J. Physiol. - Hear. Circ. Physiol.*, vol. 288, pp. 1324–1330, 2005, doi: 10.1152/ajpheart.00813.2004.

[89] G. Sommer *et al.*, “Biomechanical properties and microstructure of human ventricular myocardium,” *Acta Biomater.*, vol. 24, no. June 2016, pp. 172–192, 2015.

[90] D. S. Li *et al.*, “Insights into the passive mechanical behavior of left ventricular myocardium using a robust constitutive model based on full 3D kinematics,” *J. Mech. Behav. Biomed. Mater.*, vol. 103, no. November 2019, p. 103508, 2020, doi: 10.1016/j.jmbbm.2019.103508.

[91] W. Y. I. Tseng, J. Dou, T. G. Reese, and J. Van Wedeen, “Imaging myocardial

fiber disarray and intramural strain hypokinesis in hypertrophic cardiomyopathy with MRI," *J. Magn. Reson. Imaging*, vol. 23, no. 1, pp. 1–8, 2006, doi: 10.1002/jmri.20473.

[92] R. Ariga *et al.*, "Identification of Myocardial Disarray in Patients With Hypertrophic Cardiomyopathy and Ventricular Arrhythmias," *J. Am. Coll. Cardiol.*, vol. 73, no. 20, pp. 2493–2502, 2019, doi: 10.1016/j.jacc.2019.02.065.

[93] F. Pashakhanloo *et al.*, "Submillimeter diffusion tensor imaging and late gadolinium enhancement cardiovascular magnetic resonance of chronic myocardial infarction," *J. Cardiovasc. Magn. Reson.*, pp. 1–14, 2017, doi: 10.1186/s12968-016-0317-3.

[94] M. Pop *et al.*, "Quantification of fibrosis in infarcted swine hearts by ex vivo late gadolinium-enhancement and diffusion-weighted MRI methods," *Phys. Med. Biol.*, vol. 58, no. 15, pp. 5009–5028, 2013, doi: 10.1088/0031-9155/58/15/5009.

[95] G. L. Kung *et al.*, "Microstructural remodeling in the post-infarct porcine heart measured by diffusion tensor MRI and T1-weighted late gadolinium enhancement MRI," *J. Cardiovasc. Magn. Reson.*, vol. 14, no. S1, pp. 2–4, 2012, doi: 10.1186/1532-429x-14-s1-p66.

[96] E. X. Wu *et al.*, "MR diffusion tensor imaging study of postinfarct myocardium structural remodeling in a porcine model," *Magn. Reson. Med.*, vol. 58, no. 4, pp. 687–695, 2007, doi: 10.1002/mrm.21350.

[97] M. T. Wu *et al.*, "Sequential changes of myocardial microstructure in patients postmyocardial infarction by diffusion-tensor cardiac mr correlation with left

ventricular structure and function," *Circ. Cardiovasc. Imaging*, vol. 2, no. 1, pp. 32–40, 2009, doi: 10.1161/CIRCIMAGING.108.778902.

[98] T. Rahman, K. Moulin, D. B. Ennis, and L. E. Perotti, "Diffusion Biomarkers in Chronic Myocardial Infarction," *Lect. Notes Comput. Sci. (including Subser. Lect. Notes Artif. Intell. Lect. Notes Bioinformatics)*, vol. 12738 LNCS, pp. 137–147, Jun. 2021, doi: 10.1007/978-3-030-78710-3_14.

[99] W. Holmes, J. A. Nunez, J. W. Covell, W. Jeffrey, J. A. Nufiez, and W. James, "Functional implications of myocardial scar structure," *Am. J. Physiol. - Hear. Circ. Physiol.*, 1997.

[100] J. C. Walker *et al.*, "Helical myofiber orientation after myocardial infarction and left ventricular surgical restoration in sheep," *J. Thorac. Cardiovasc. Surg.*, vol. 129, no. 2, pp. 382–390, 2005.

[101] D. E. Sosnovik *et al.*, "Diffusion spectrum mri tractography reveals the presence of a complex network of residual myofibers in infarcted myocardium," *Circ. Cardiovasc. Imaging*, 2009, doi: 10.1161/CIRCIMAGING.108.815050.

[102] L. A. McGill *et al.*, "Reproducibility of in-vivo diffusion tensor cardiovascular magnetic resonance in hypertrophic cardiomyopathy," *J. Cardiovasc. Magn. Reson.*, vol. 14, no. 1, pp. 1–15, 2012, doi: 10.1186/1532-429X-14-86.

[103] B. Le *et al.*, "Microarchitecture of the Hearts in Term and Former-Preterm Lambs using Diffusion Tensor Imaging," *Anat. Rec.*, no. May 2020, pp. 803–817, 2020, doi: 10.1002/ar.24516.

[104] Y. J. Cheng, D. Lang, S. D. Caruthers, I. R. Efimov, J. Chen, and S. A. Wickline, "Focal but reversible diastolic sheet dysfunction reflects regional calcium mishandling in dystrophic mdx mouse hearts," *Am. J. Physiol. - Hear. Circ. Physiol.*, vol. 303, no. 5, 2012, doi: 10.1152/ajpheart.00321.2012.

[105] A. Das *et al.*, "Acute Microstructural Changes after ST-Segment Elevation Myocardial Infarction Assessed with Diffusion Tensor Imaging," *Radiology*, p. 203208, 2021, doi: 10.1148/radiol.2021203208.

[106] R. R. Edelman *et al.*, "In vivo measurement of water diffusion in the human heart," *Magn. Reson. Med.*, vol. 32, no. 3, pp. 423–428, 1994, doi: 10.1002/mrm.1910320320.

[107] K. Moulin *et al.*, "In vivo free-breathing DTI and IVIM of the whole human heart using a real-time slice-followed SE-EPI navigator-based sequence: A reproducibility study in healthy volunteers," *Magn. Reson. Med.*, vol. 76, no. 1, pp. 70–82, 2016, doi: 10.1002/mrm.25852.

[108] T. G. Reese, R. M. Weisskoff, R. N. Smith, B. R. Rosen, R. E. Dinsmore, and V. J. Wedeen, "Imaging myocardial fiber architecture in vivo with magnetic resonance," *Magn. Reson. Med.*, vol. 34, no. 6, pp. 786–791, 1995.

[109] S. Rapacchi *et al.*, "Low b-Value Diffusion-Weighted Cardiac Magnetic Resonance Imaging," *Invest. Radiol.*, vol. 46, no. 12, pp. 751–758, 2011, doi: 10.1097/RLI.0b013e31822438e8.Low.

[110] M. Froeling, G. J. Strijkers, A. J. Nederveen, and P. R. Luijten, "Whole heart DTI using asymmetric bipolar diffusion gradients," *J. Cardiovasc. Magn. Reson.*, vol.

17, no. S1, pp. 1–2, 2015, doi: 10.1186/1532-429x-17-s1-p15.

[111] C. L. Welsh, E. V. R. Di Bella, and E. W. Hsu, “Higher-Order Motion-Compensation for in Vivo Cardiac Diffusion Tensor Imaging in Rats,” *IEEE Trans. Med. Imaging*, vol. 34, no. 9, pp. 1843–1853, 2015, doi: 10.1109/TMI.2015.2411571.

[112] L. E. Perotti *et al.*, “Estimating cardiomyofiber strain in vivo by solving a computational model,” *Med. Image Anal.*, vol. 68, 2021, doi: 10.1016/j.media.2020.101932.